

Contents — N through O

Synoptic Seasonal Structure Evolution of the Low-Latitude Cloud Belt <i>T. Nakakushi, T. Akabane, K. Iwasaki, and S. M. Larson</i>	3118
Magmas Parental to the Chassigny Meteorite: New Considerations <i>H. Nekvasil, J. Filiberto, M. Whitaker, and D. H. Lindsley</i>	3041
Multiyear Simulations of the Martian Water Cycle with the Ames General Circulation Model <i>S. M. Nelli, J. R. Murphy, R. M. Haberle, and J. R. Schaeffer</i>	3169
Characteristics of Mini-Magnetospheres Formed by Paleo-Magnetic Fields of Mars <i>N. F. Ness, A. M. Krymskii, D. H. Crider, T. K. Breus, M. H. Acuna, D. Hinson, and K. K. Barashyan</i>	3119
Polar Dunes Resolved by the Mars Orbiter Laser Altimeter Gridded Topography and Pulse Widths <i>G. A. Neumann</i>	3262
Fluvial and Lacustrine Processes in Meridiani Planum and the Origin of the Hematite by Aqueous Alteration <i>H. E. Newsom, C. A. Barber, R. T. Schelble, T. M. Hare, W. C. Feldman, V. Sutherland, A. Livingston, and K. Lewis</i>	3233
First Planetary Rock Coring in Our Solar System...ESA 2003 Beagle 2 Mars Lander <i>T. C. Ng, K. L. Yung, C. H. Yu, and C. C. Chan</i>	3035
The Nature of the Martian Aqueous Environments Recorded by ALH84001 Carbonates <i>P. B. Niles, L. A. Leshin, and Y. Guan</i>	3140
MGS/TES-Odyssey/THEMIS-IR Analysis of Localized Low Albedo Regions in Valles Marineris <i>E. Z. Noe Dobra, J. F. Bell III, M. J. Wolff, and K. J. Snook</i>	3179
Seasonal/Diurnal Mapping of Ozone and Water in the Martian Atmosphere <i>R. E. Novak, M. J. Mumma, M. A. DiSanti, N. Dello Russo, K. Magee-Sauer, and B. Bonev</i>	3210
Evidence for a Surging Ice-Sheet in Elysium Planitia, Mars <i>J. Nussbaumer, R. Jaumann, and E. Hauber</i>	3018
Melting of the Martian Permafrost by Hydrothermal Convection Associated with Magmatic Intrusion <i>Y. Ogawa, Y. Yamagishi, and K. Kurita</i>	3095
Subsurface Exploration for Water on Mars <i>G. R. Olhoeft</i>	3213
Mars Electromagnetic Sounding Experiment (MARSSES): Comparative and Calibration Studies on the Example Spatial and Temporal Variations Subsurface Geoelectrical Sections of the Saltwater Interface on Sicily (Donnalucata Beach) and Shelter Island <i>Y. R. Ozorovich, A. K. Lukomski, B. V. Zoubkov, and F. V. Babkin</i>	3026

SYNOPTIC SEASONAL STRUCTURE EVOLUTION OF THE LOW-LATITUDE CLOUD BELT. T. Nakakushi¹, T. Akabane², K. Iwasaki³ and S. M. Larson⁴, ¹Graduate School of Human and Environmental Studies, Kyoto University (e-mail to kushio@gaia.h.kyoto-u.ac.jp), ²Shinshu University, ³Kyoto-Gakuen University, ⁴Lunar and Planetary Laboratory, University of Arizona.

Introduction: Recently, the importance of the role of water vapor and/or ice clouds has been recently emphasized, though their activities had not been examined in the post-Viking years. Among them, the most important substances are the polar caps and the low-latitude cloud belt which appears in northern summer. It has been widely accepted that this cloud belt should be coupled with the ascending branch of the "cross-equatorial Hadley circulation" which forms in the solstitial seasons. A revolutionary development of observation techniques/devices (including spacecraft) in the latter half of the 20th century allowed us to examine the appearance and activated behavior of the cloud belt. Few of the observational reports, however, have discussed its dissipating behavior [e.g., 1,2,3], and our knowledge about it has come mostly from theoretical methods. The paucity of reports on this issue prompted us to investigate it based on observations. By combining this dissipating behavior with the previously known developing/mature state, this study attempts to give an entire story of the cloud belt, and of the Martian climate.

Observations: This is a brief report on the Martian climate, based on our ground-based observations in 1997, 1999, and 2001. The focus is the entire synoptic behavior and evolution of the low-latitude cloud belt appearing around the aphelion. The 1997 and 1999 observations are very suitable for the mature state of the cloud belt. The first half of the 2001 apparition corresponded to the northern late summer/early autumn on Mars. It was suitable for studying the dissipating behavior, and especially for studying the latitudinal coverage of the cloud belt, because we could observe Mars from "equator-on" views, that is, the sub-Earth point was almost on the equator in this apparition. The telescope which we used in 1997 was the 65 cm refractor at Hida Observatory, Japan. Those in 1999 and 2001 were the Steward Observatory Mt. Lemmon 60 inch and Catalina 61 inch telescopes in Arizona, U.S.A. Image pixel sizes range from 0."08 to 0."18. All of the images were blue-filtered (less wavelengths than 440nm, with narrow-band filters). We restrict the following discussion to this wavelength accordingly.

The bias subtraction and flat fielding were performed using the astronomical standard Image Reduction and Analysis Facility (IRAF) software package. IRAF is distributed by National Astronomy Observatories (NOAO), which is operated by the Association of Universities for Research in Astronomy, Inc., under contract to the National Science Foundation.

Diurnal Variation of Water Ice Cloud Opacity: We present in this section the results of measuring the water ice optical thickness in blue light. We define here a cloud "belt" as wholly encircling the tropics, and a cloud "band" as a cluster of WICs covering broad areas of the tropics. Our WIC-opacity estimation algorithm is based on the "discrete-ordinate" method. The parameters adopted here were as follows: the Minnaert exponent, $k = 0.53$ [4, for small phase angles]; the ground normal albedo, $A_n = 0.06$ [5]; the opacity of CO₂ atmosphere and that of dust were assumed to be 0.01 [6], and 0.3 [7,8], respectively. All of these values, and also hereafter, were treated as those in blue (~440nm) according to our observations. The phase function for water ice particles used here was that of Clancy and Lee [9]. In this paper, the region of interest on this WIC opacity estimation is Arabia, centered at (315°W, 10°N). For further details and other information, the reader may refer to our previous papers, where it was also demonstrated that the constancy of dust opacity (=0.3) does not greatly affect the opacity estimation of WICs [8,10,11, and references therein].

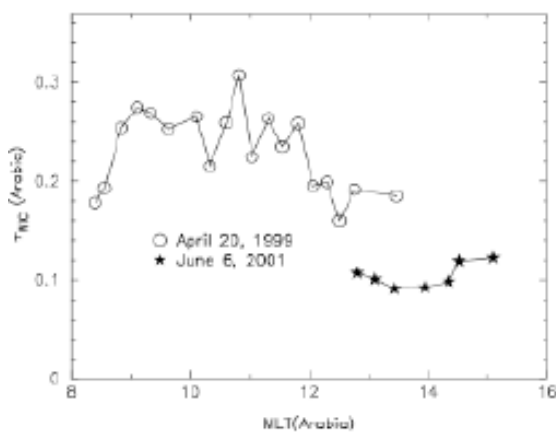


Figure 1. (left) Diurnal variations of WIC opacities in 1999 and 2001.

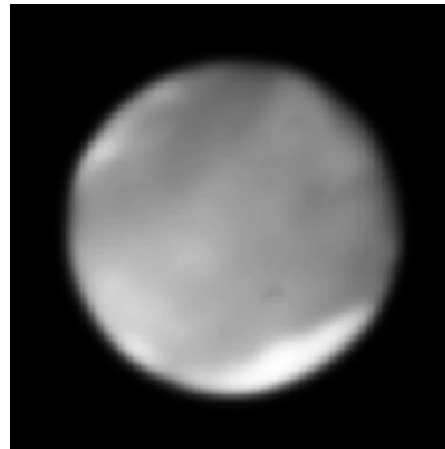


Figure 2. (right) Sample image taken on 2001 June 6. A faint, broad cloud band can be seen (the sub-Earth point longitude is 33°W). The contrast is slightly enhanced.

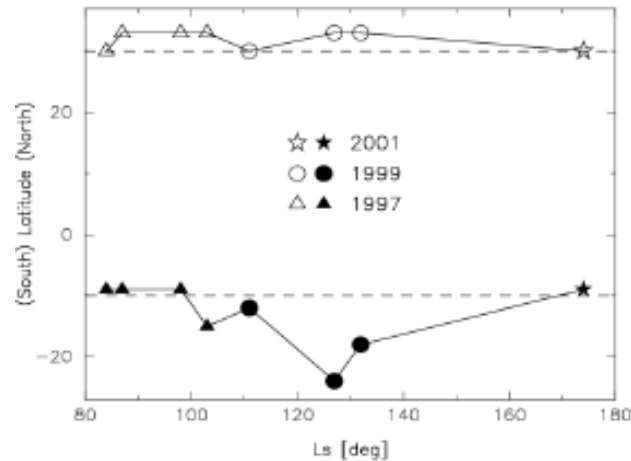


Figure 3. Northern/southern limits. The dashed lines at 30°N and 10°S show those suggested by Clancy et al. [14].

Figure 1 depicts the derived diurnal variation of the WIC opacity on 2001 June 6 ($L_s = 174^{\circ}$). Figure 2 is a sample image. For a comparison, results from similar calculations for 1999 April 20 ($L_s = 127^{\circ}$) are included in the figure. The WIC band on this day can be seen in Figure 1 of Nakakushi et al. [10].

The WIC opacities at $L_s = 174^{\circ}$ in Figure 1 are much smaller than at $L_s = 127^{\circ}$. The factor is $\sim 1/2$ at around 1300MLT (Martian Local Time). Although these results show that the cloud band was significantly weakened at $L_s = 174^{\circ}$ in 2001, we emphasize here the existence, itself, of the cloud band of moderate dimension (as seen in Figure 2) with an opacity of ~ 0.1 as late as at $L_s = 174^{\circ}$. However, the "faint" cloud band may be a kind of "visual product" and it may not be real; the existence of the morning clouds, which form the morning part of the cloud belt, is clearly recognized (on the left side limb of the Mars disk in the figure), so that the results presented in this paper will not be seriously damaged by this uncertainty. The existence of the cloud belt/band will be justified by upcoming reports on spacecraft observations. Smith and Lemmon [12] also showed the presence of WIC(s) during the Mars Pathfinder mission ($L_s = 142^{\circ}$ - 188° in 1997). However, their result doesn't imply the presence of the WIC *belt* (nor *band*), as shown in Figure 2. A reanalysis of Viking data sets [13] also shows evidence for clouds in the equatorial region between $L_s = 110^{\circ}$ - 170° , though the spatial coverage of the data is not complete.

Latitudinal Coverage of the Cloud Belt: There have been several works which indicate that the aphelion cloud belt usually covers the tropical zone of 30°N - 10°S [e.g., 13,14]. We examined the L_s -dependence of the latitudinal distribution of the cloud band using images obtained in these three apparitions: 1997, 1999, and 2001. The presence of WICs can be discerned in blue(violet)-filtered images. We first obtained the brightness distribution of each image. For this analysis the data points used were confined within 1100-1300MLT (i.e., around the sub-solar point), that is, we neglected the dependence of the WIC distribution on the topography. The grid-point spacing was 3° by 3° . These brightness data were then longitudinally averaged. The averaged brightness data were plotted as a function of the latitude. Finally, we defined the latitude which gave the maximum second-order differential of the brightness curve as the "northern/southern limit latitude."

The obtained L_s -dependence of the northern and southern limit latitudes of the cloud band (belt) is presented in figure 3. The northern limit of the cloud band does not show any significant L_s -dependence, while the southern one expands around $L_s \sim 120^{\circ}$ - 130° . This southern limit expansion, however, may be due to low resolution on the observations, and/or due to the inclination of the Martian rotation axis to Earth, in the 1999 apparition. However, we note that the latitudinal coverage of the band shows no significant "shrinking" toward the dissipation. This suggests that the cloud band has a minimum latitudinal dimension. Wolff et al. [15] suggested that the band's dissipation occurred at $L_s \sim 146^{\circ}$ in 1997. Smith et al. [2] suggested that it occurred near $L_s = 145^{\circ}$ in 1999. Both saw clouds between 30°N and 10°S . In the 2001 apparition, the public image of Mars taken with HST on June 26 with the 410nm filter apparently suggests that the bands no longer existed by $L_s \sim 185^{\circ}$ (press-released HST images, including this image of Mars, are available from the World Wide Web server for the STScI at <http://www.stsci.edu/>). We could not find any significant low-latitude WIC belt/bands in our images at $L_s = 178^{\circ}$ (2001 June 15). The comparison of Figure 3 to these solar longitudes of dissipation for each year suggests that the band (belt) had never reduced its dimension to under the 30°N - 10°S latitudinal range until its end.

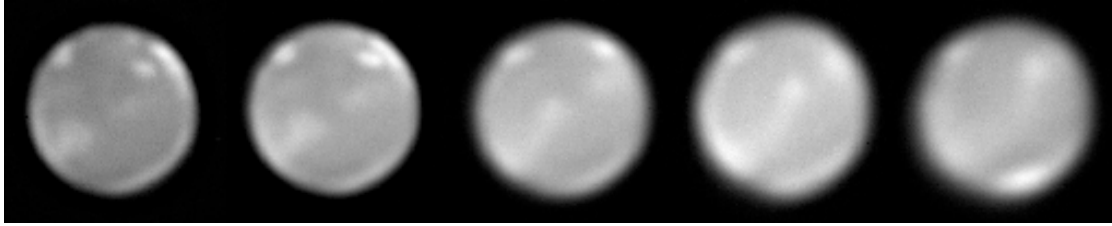


Figure 4. Images on 1999 April 27. The upper-left direction is north on Mars. The longitudes of the sub-Earth point (LON_{SE}) are 181° , 191° , 212° , 232° , and 256° , respectively (left to right). Within the image of $LON_{SE} = 181^\circ$, we can see a large orographic cloud over Elysium in the morning side, a large faint cloud near Amazonis on early afternoon, a bright Olympus orographic cloud in the evening, and a bright WIC zone on the dusk limb. The WIC band is (or appears to be) led by the Elysium cloud(s).

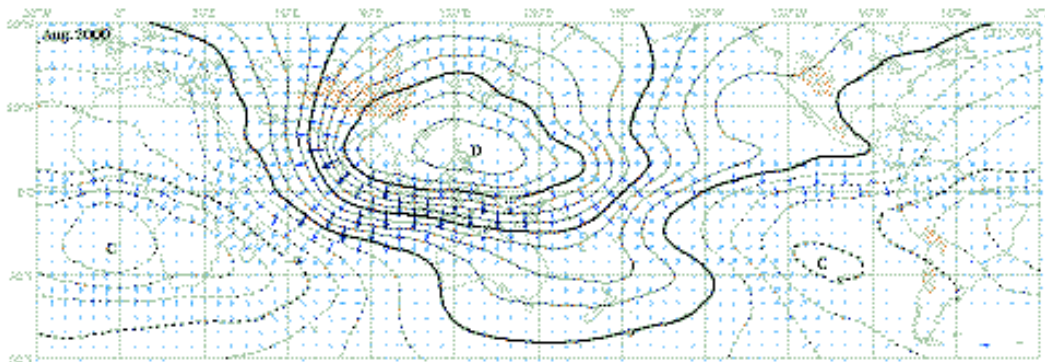


Figure 5. Monthly mean (2000 August) 200 hPa velocity potential (contours) and divergent wind vector (blue arrows) on Earth [17]. The divergence and convergence are represented as "D" and "C", respectively, in units of $10^6 \text{ s}^{-1} \text{ m}^2$. The longest arrow indicates 4 ms^{-1} . Since the 200 hPa level corresponds to that near the tropopause on Earth, the divergence (convergence) zones can be regarded as the rising (sinking) branches of the Hadley cells.

Remarks and Summary: On 1999 April 27 ($L_s = 130^\circ$), the planetary encircling WIC belt had divided into a "semi-encircling" band (led by the Elysium orographic cloud) and a discrete cloud centered at around (170°W , 10°N), southwest of Amazonis (see Figure 4), whereas some orographic clouds were present. Our images taken on 1999 February 28 ($L_s = 104^\circ$) show a similar situation. This $L_s = 104^\circ$ period is the time when the cloud belt (or cloud bands) should show its (their) strong (maybe strongest) activity. An HST cylindrical map image [e.g., 14] presents the cloud belt in its mature state at $L_s = 68^\circ$ in 1995. We notice less cloudiness around 180°W on the HST map image, though no corrections for cloud limb brightening had been applied to the map. Our images at $L_s = 95^\circ$ (1997 March 24) also show the mature cloud belt even around the Amazonis area [16, their Figure 2]. Plate 3 of Tamppari et al. [13] suggests the presence of the belt/bands/clouds until $L_s \sim 120^\circ\text{-}140^\circ$. Moreover, though they did discuss clouds associated with topography, their results still need closer investigations in terms of this issue of the WIC division/dissipation behavior. Although we can not apparently identify the bands in our images on 2001 June 15 ($L_s = 178^\circ$) due to their being too faint and/or due to the occurrence of the blue clearing in the Syrtis Major region, there might remain a faint, but modestly large, cloud over Arabia with a similar latitudinal dimension. The directly inferred dissipating behavior is summarized as followed: (1) The cloud belt is already in its full-encircling mature state by $L_s = 84^\circ$, and so continues the state until $L_s \sim 100^\circ$. (2) The belt gradually divides into semi-encircling band(s) and discrete WIC(s) around $L_s \sim 100^\circ\text{-}110^\circ$. Although this division may not occur apparently if the belt's activity is too strong, the cloud activity may be expected to localize. (3) The clouds/cloud bands fade away towards the equinox without prominent latitudinal shrinkage.

Many theoretical studies have predicted a cross-equatorial Hadley cell from the summer hemisphere to the winter hemisphere in seasons including the solstices [e.g., 18]. Clancy et al. [14] suggested that the northern summer ascending branch of this cross-equatorial Hadley cell is embodied in the low-latitude cloud belt. Our Figure 3 therefore indicates that the Hadley cell keeps its minimum dimension at least while the cloud band is alive. The division (or "discretization") of the cloud band pointed out above may imply localization of the Hadley circulation. Local Hadley cells are also suggested on Earth [17; see Figure 5], though their properties and causes may probably be different from the expected Martian ones.

On the other hand, we have discussed the mature and dissipating behaviors of the belt, and its relation to the orographic and evening/morning clouds [8,10,11]. Accordingly, we proposed that (1) morning clouds which do not dissipate even in midday due to the growing Hadley circulation and the decreasing solar insolation should tie to evening clouds, forming the cloud belt: (2) the belt should localize longitudinally in the dissipating phase.

These apparently inconsistent theories may be consistently connected by the effects of atmospheric waves, thermal tides in particular, which is proposed in this article. Morning/evening clouds can be recognized firstly to be formed in convergent/upwelling and/or cool regions due to prominence of a semidiurnal tide. This effect should be more prominent by superimposing the increasing Hadley circulation, which forms the cloud belt. In the dissipation, the inverted processes should make the localization of the cloud belt and the background

Hadley circulation. Although this idea surely requires more investigation, the outline of the story that tells the superimposition of large-scale atmospheric waves onto the cross-equatorial Hadley circulation. "Waves" may be the key to the cloud belt.

In the 2001 apparition, the cloud belt was alive at $L_s = 174^\circ$ with an optical depth of ~ 0.1 , and its end was around $L_s \sim 180^\circ$. Reportedly, a global dust storm rose from the Hellas Basin just after the belt's/band's dissipation ($L_s \sim 180^\circ$ - 190°) in 2001 [e.g., public GIF images from MGS (Mars Global Surveyor) TES (Thermal Emission Spectrometer), personal communication with Christensen et al. of Arizona State University]. This seems unusually early for large-scale dust storms. The storm became the largest in several decades and it wrapped the entire planet for several months. These facts urge us to hypothesize that there is some connection between the strong and long-lasting activity of the WIC bands in the 2001 northern summer and the strong and long-lasting activity of the dust storm. An investigation of this relationship will be a part of future studies in order to clarify the interannual and seasonal variations of the Martian climate.

References: [1] Pearl J. C., Smith M. D., Conrath B. J., Bandfield J. L., and Christensen P. R. (2001) *J. Geophys. Res.*, *106*, 12,325-12,338. [2] Smith M. D., Pearl J. C., Conrath B. J., and Christensen P. R. (2001) *J. Geophys. Res.*, *106*, 23,929-23,945. [3] Wang H. and Ingersoll A. P. (2002) *J. Geophys. Res.*, *107*, doi:10.1029/2001JE001815, 5078. [4] Erard S. (2000) , *Planet. Space Sci.*, *48*, 1271-1287. [5] Akabane T., Iwasaki K., Saito Y., and Narumi Y. (1987) *Publ. Atron. Soc. Jpn.*, *39*, 343-359. [6] Wells R. A. (1979) *Geophysics of Mars* (New York: Elsevier Sci.), ch. 2, p. 125-338. [7] Clancy R. T., Sandor B. J., Wolff M. J., Christensen P. R., Smith M. D., Pearl J. C., Conrath B. J., and Wilson R. J. (2000) *J. Geophys. Res.*, *105*, 9553-9571. [8] Akabane T., Nakakushi T., Iwasaki K., and Larson S. M. (2002), *A&A*, *384*, 678-688. [9] Clancy R. T., and Lee S. W. (1991) *Icarus*, *93*, 135-158. [10] Nakakushi T., Akabane T., Iwasaki K., and Larson S. M. (2001) *J. Geophys. Res.*, *106*, 5043-5056. [11] Nakakushi, T., Akabane T., Iwasaki K., and Larson S. M. (2002) *Publ. Atron. Soc. Jpn.*, *54*, L31-L34. [12] Smith P. H., and Lemmon M. (1999) *J. Geophys. Res.*, *104*, 8975-8985. [13] Tamppari L. K., Zurek R. W., and Paige D. A. (2000) *J. Geophys. Res.*, *105*, 4087-4107. [14] Clancy R. T., Grossman A. W., Wolff M. J., James P. B., Rudy D. J., Billawala Y. N., Sandor B. J., Lee S. W., and Muhleman D. O. (1996) *Icarus*, *122*, 36-62. [15] Wolff M. J., Bell J. F. III, James P. B., Clancy R. T., and Lee S. W. (1999) *J. Geophys. Res.*, *104*, 9027-9041. [16] Akabane T., Nakakushi T., Iwasaki K., and Larson, S. (1999), in *The 32nd ISAS Lunar and Planetary Symposium* (Kanagawa: Inst. of Space and Astron. Sci.), 192-195. [17] Japan Meteorological Agency (2001) *Annual Report on Climate System 2000* [CD-ROM] (Japan Meteorol. Business Support Cent.). [18] Haberle R. M., Pollack J. B., Barnes J. R., Zurek R. W., Leovy C. B., Murphy J. R., Lee, H., and Schaeffer J. (1993) *J. Geophys. Res.*, *98*, 3093-3123.

Additional Information: The first author (TN) is supported by the Research Fellowships of the Japan Society for the Promotion of Science for Young Scientists.

MAGMAS PARENTAL TO THE CHASSIGNY METEORITE: NEW CONSIDERATIONS. H. Nekvasil¹, J. Filiberto¹, M. Whitaker¹, and D.H. Lindsley¹, ¹Department of Geosciences, State University of New York, Stony Brook, NY 11794-2100, Hanna.Nekvasil@sunysb.edu.

Introduction: Comparisons with plume-associated magmas on Earth suggest major similarities between the Chassigny mineral assemblages and those that fractionate along the *hy*(hypersthene)-normative sodic alkalic trend exemplified by lavas from certain ocean island, continental hotspot and continental rift regimes.

Plume-associated magmas on Earth are characterized by extreme diversity of associated rocks, with rocks ranging from alkali basalt, olivine tholeiite, and biotite gabbro to anorthosite, syenite, comendite, pantellerite, phonolite and potassic granite, and spanning the spectrum from silica-undersaturated to silica-oversaturated units, including peralkaline types. However, viewed globally, plume-associated magmatic suites, as defined by spatially and temporally associated rock units, fall into distinct patterns. These patterns emerge as four major trends (Fig. 1a).

Trend 1 shows the variation in bulk lava compositions of the sodic *hy*-normative mildly alkalic suites as a function of silica content. Rocks along this trend extend through the sequence alkalic basalt-hawaiite-mugearite-benmoreite-trachyte-rhyolite with occasional peralkaline members. This trend is exemplified by rock suites from Ascension Island [1] and the Azores [2]. Figure 1a shows that rock units within these suites are clearly alkalic according to the classification scheme of Irvine and Baragar [3], yet are not silica-undersaturated and differ distinctly from the alkalic rocks typical of ocean island such as Hawaii (Trend 4).

Trend 2 shows the variation in lava compositions of *hy*-normative potassic suites with silica content. These suites include fine-grained rocks of the Proterozoic anorthosite complexes and make up the sequence biotite gabbro-ferrodiorite (jotunite)-monzodiorite- monzonite-monzosyenite-syenite-and potassic granite [4]. Volcanic equivalents appear to be given by the basalt-ferrobasalts-trachyte-potassic rhyolite of the Snake River Plain [5,6]. This trend is characterized by rocks with low silica and alumina that contain as much as 25 wt% FeO_T and are strongly enriched in Ti and P as well as silica-rich rocks (i.e. potassic granites) with high Fe/Mg ratios. Also distinctive is the subalkalic nature of the least evolved rocks, but alkalic nature of the intermediate rocks.

Trend 3 reflects the typical subalkalic tholeiitic provinces of ocean islands such as Iceland with their olivine tholeiite-ferrobasalt-icelandite-sodic rhyolite sequences [7]. Trend 4 is more diffuse and less well defined, but includes the silica-undersaturated alkali

basalt - *ne*-hawaiite - *ne*-mugearite - phonolite sequence as well as the nephelinites of Hawaii, Tristan da Cunha, and Gough Island [8]. This trend typifies what most petrologists refer to as "alkalic".

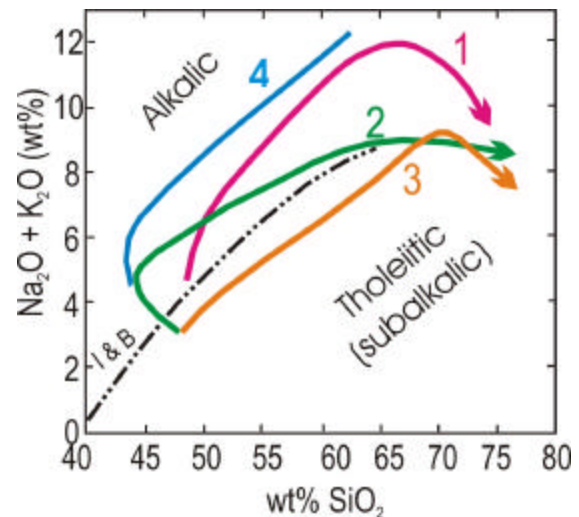


Figure 1a. Four primary trends of bulk rocks in plume-associated magmatic suites.

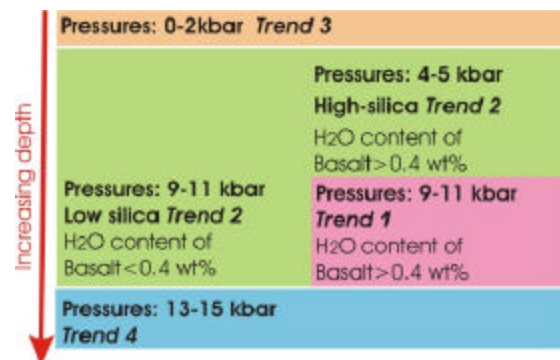


Figure 1b. Conditions under which each of the trends of Figure 1a have been reproduced experimentally by fractionation.

Experiments have been conducted on each of these trends in order to assess how much of the compositional diversity seen in each trend could be ascribed to fractionation [9-14]. These experiments simulated crystal fractionation by incrementally using residual liquids as the new bulk compositions. They have provided a map of the conditions of pressure and water contents that produce the assemblages that lead to these liquid trends (Fig. 1b). The results of these experiments pro-

vide a foundation upon which to evaluate the assemblages of the Chassigny meteorite.

Relation to the Chassigny cumulate and inclusion assemblages: The Chassigny dunite consisting of unzoned Fe_{68} with possible cumulate augite, $En_{50}Wo_{34}Fs_{16}$ (mol%), pigeonite, $En_{63}Wo_{12}Fs_{25}$, and unexsolved orthopyroxene $En_{68}Wo_4Fs_{28}$ [15]. According to QUIIF [16] calculations, this assemblage could be in equilibrium at $\sim 1050^\circ C$ (at pressures within the range 1-9 kbar), although the pigeonite appears metastable at this temperature. Evidence for a lower temperature assemblage appears preserved in the intercumulus assemblage that consists primarily of pyroxene, plagioclase, ilmenite, and other oxides [15]. Melt inclusions in the olivine of the Chassigny cumulate assemblage contain the additional assemblage kaersutite, augite, low-Ca pyroxene, chlorapatite, chromite, and silica-rich glass [15, 17]. QUIIF calculations on inclusion pyroxene and the olivine host suggest possible equilibrium between hosting olivine and inclusion pyroxenes and oxides in the Chassigny (albeit, under oxidized conditions - $\log fO_2$ of 2.5 log units above FMQ).

Non-feldspathic glass in polyphase melt inclusions of the Chassigny meteorite [18] is of particular interest. Shown in red in Figure 2, this glass is an alkali-rich rhyolite and has remarkable similarities to the rhyolites of suites of the hy-normative alkalic trend (Trend 1 of Fig. 1a) exemplified in Figure 2 by rocks from Ascension Island, the Azores, Clarion Island, Mexico and the Nandewar volcano of N.S.W. Australia. The conditions under which fractionation could lead to the primary chemical diversity of rocks within this trend has been the focus of recent fractionation experiments by our group and data are now available for direct comparison with the cumulate and melt-inclusion assemblage.

Figure 3 shows experimental glass compositions (gray symbols) from fractionation experiments conducted on natural lavas (black symbols) from the Nandewar volcano at 9.3 kbar and 2 wt% initial bulk water content, starting with a mildly alkalic hawaiiite. Experimental mineral assemblages along the experimental fractionation path are shown in Table 1. All of the phases observed in the cumulate and inclusion assemblages of the Chassigny meteorite were obtained experimentally (olivine, orthopyroxene, clinopyroxene, kaersutite, apatite and late-stage plagioclase and ilmenite). Ti-biotite was obtained when the water contents of the least evolved hawaiiite along the path was slightly less than 2 wt%. Upon comparison of experimental mineral compositions with those of the Chassigny cumulate assemblage, it is clear that within the temperature range 1080-1040°C, which bridges the temperature obtained independently through QUIIF calcu-

lations ($1050^\circ C$), experimental mineral compositions bracket those of Chassigny (Table 1).

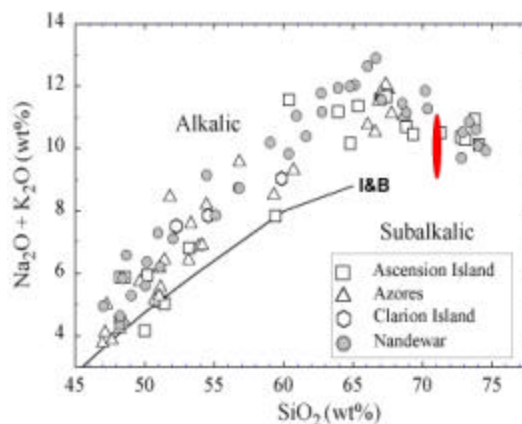


Figure 2. Total alkalis vs. silica for the Chassigny non-feldspathic glass of polyphase melt inclusions (Johnson et al., 1991) compared with natural bulk lava compositions along Trend 1 of Figure 1. The curve labeled I&B is the alkalic/subalkalic boundary of Irvine and Baragar (1971).

$T^\circ C$	Experimental Assemblage at 9.3kbar; 2 wt% H_2O	Chassigny Cumulate Assemblage
1200	Olivine (Fe_{82})	
1080	Olivine (Fe_{72}) Clinopyroxene ($En_{54}Wo_{32}Fs_{14}$)	
1050?		Olivine (Fe_{68}) Clinopyroxene ($En_{50}Wo_{34}Fs_{16}$) Orthopyroxene ($En_{68}Wo_4Fs_{28}$)
1040	Clinopyroxene ($En_{48}Wo_{28}Fs_{24}$) Orthopyroxene ($En_{62}Wo_5Fs_{33}$) Kaers + Ap	
1020	Orthopyroxene ($En_{61}Wo_4Fs_{35}$) Kaers + Ap	
950	Kaers + Ap + Il Plagioclase ($An_{24}Ab_{65}Or_7$)	

Table 1. Experimental mineral assemblages and compositions compared to those of the the cumulate assemblage of Chassigny at the QUIIF temperature of $1050^\circ C$. Arrows connect like phases for ease of comparison.

Shown in green in Figure 3 is the trachyandesite liquid composition at $1040^\circ C$ that is in equilibrium with

the experimental mineral compositions listed in Table 1. This liquid could readily fractionate to the rhyolitic glass of Chassigny (shown in red) at 9.3 kbar, producing in the process, volumetrically abundant kaersutite.

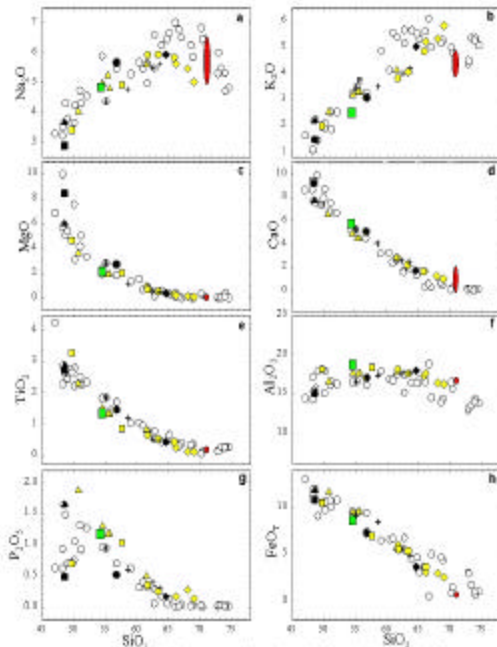


Figure 3. Experimental glass compositions along the fractionation path of a Nandewar basaltite at 9.3 kbar and 2 wt% initial bulk water content (yellow symbols). *Black:* Starting compositions for the fractionation steps. *Clear:* Bulk compositions of lavas from the Nandewar suite (Trend 1). *Red:* Non-ferridaphnic glass in the Chassigny polyphase melt inclusions. *Green:* Experimental liquid at 1040°C.

Pyroxene compositions of the Chassigny meteorite also give information about potential pressures of fractionation. Figure 4 shows the Al:Ti cation ratios of experimental clinopyroxenes as a function of pressure, natural clinopyroxenes from the Nandewar rocks, and Chassigny inclusion pyroxenes (in red) [18]. The Chassigny clinopyroxenes are fully consistent with fractionation at ~9 kbar.

If the Chassigny assemblage can indeed be reproduced by crystallization along Trend 1, as suggested by our evaluation above, then a variety of implications arise.

- The magma trapped in the olivine (represented now by polyphase melt inclusions) and in equilibrium with the co-existing "cumulate" clino- and orthopyroxene could be similar to basaltic trachyandesite of the mildly alkalic *hy*-normative magmatic suites on Earth.
- Parental to the basaltic trachyandesite melt that can produce the Chassigny cumulate assemblage is mildly alkalic *hy*-normative hawaiite. [Importantly, this is not an alkali basalt since it is *not* normative and hence, not silica-undersaturated.]

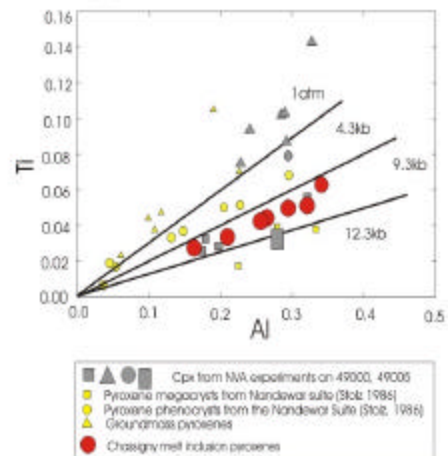


Figure 4. Ti:Al cation abundances in Chassigny melt inclusion clinopyroxene (red; Johnson et al., 1991). Heavy lines separate regions defined by experiments (gray symbols) of Nekvasil et al. (in review). The polybaric nature of natural pyroxenes of such suites are shown by natural pyroxenes of the Nandewar suite (yellow).

- On Earth, such parental magmas have low Mg#s due to earlier fractionation histories. For this reason, the low Mg#s of the Chassigny assemblages cannot be used to support the concept of a martian mantle that is more Fe-rich than that on Earth.
- Further fractionation of the trachyandesite would give rise to volumetrically abundant trachyte and finally rhyolite of the variety found as glass within the polyphase melt inclusions of the Chassigny meteorite.
- Magmatic water contents needed to produce the Chassigny assemblages lies between 0.4 and 2 wt%.
- Although the silica content of basaltic trachyandesite (i.e., the suggested Chassigny assemblage host magma) is consistent with the mafic material of Surface Type 1 of the martian southern highlands suggested by deconvoluted TES spectra [19], the alkali content of a basaltic trachyandesite is significantly higher.
- Fractionation of basaltic trachyandesite would produce volumetrically abundant trachyandesite with silica contents of the Surface Type 2 of the northern lowlands, but again lower alkali contents.

- The fractionation (or ponding) pressure indicates the presence of a physical barrier to magma ascent within the upper layers of Mars. If, as on Earth, this barrier marks the crust/mantle interface, then this may provide independent estimates of the thickness of the martian crust in the regions of Elysium and Tharsis. Assuming a depth to pressure ratio of $\sim 7.7 \text{ km/kbar}$ on Mars (based on a density of 3.5 g/cm^3 for the martian upper mantle and crust and a gravitational constant of 3.7 m/s^2 [20]), this depth and therefore crustal thickness, is $\sim 70 \text{ km}$.

References: [1] Harris C. (1983) *J. Petrol.*, 27, 251-276. [2] White W.M. et al. (1979) *Contribs. Min. Petrol.*, 69, 201-213. [3] Irvine, T.N. and Baragar, W.R.A. (1971) *Can. J. Earth Sci.*, 8, 523-548. [4] Scoates, J.S. et al. (1996) *Geol. Soc. Amer. Bull.*, 108, 1357-1351. [5] Stout et al. (1994) *J. Petrol.*, 35, 1681-1715. [6] Frost, B.R. and Frost, C.D. (1997) *Geol.*, 25, 647-650. [7] Carmichael, I.S.E. (1964) *Am. Min.*, 52, 1815-1841. [8] Frey, F.A. et al. (1991) *J. Geophys. Res.*, 96, 14347-14375. [9] Nekvasil, H. et al. (2002) *Geochim. Cosmochim. Acta*, 66, Abstract, A549. [10] Dondolini, A. (2001) M.S. Thesis, Geosciences, SUNY Stony Brook. [11] Rossier, L. et al. (2001) *GSA Abstr. w. Prog.*, 33, A86. [12] Litvin, V.Y. (2002) M.S. Thesis, Geosciences, SUNY Stony Brook. [13] Litvin, V. et al. (2001) *GSA Abstr. w. Prog.*, 33, A86. [14] Nekvasil, H. et al. (2001) *GSA Abstr. w. Prog.*, 33, A87. [15] Floran, R.J. et al. (1978) *Geochim. Cosmochim. Acta*, 42, 1213-1229. [16] Andersen, D.J. et al. (1993) *Comp. & Geosc.*, 19, 1333-1350. [17] Meyer, C. (1998) *Mars Meteorite Compendium*, NASA. [18] Johnson, M.C. et al., (1991) *Geochim. et Cosmochim. Acta*, 55, 349-366. [19] Hamilton, V.E. et al. (2001) *J. Geophys. Res.*, 106, 14733-14746. [20] Lodders, K. and Fegley, B. Jr. (1998) *The Planetary Scientist's Compendium*. Oxford Univ. Press, New York.

MULTIYEAR SIMULATIONS OF THE MARTIAN WATER CYCLE WITH THE AMES GENERAL CIRCULATION MODEL. S. M. Nelli^{1,*}, J. R. Murphy¹, R. M. Haberle², and J. R. Schaeffer², ¹Department of Astronomy, New Mexico State University, P.O. Box 30001/MSC 4500, 1320 Frenger Street, Las Cruces, NM 88003-8001, USA. *e-mail address: snelli@nmsu.edu (S. M. Nelli), ²NASA-Ames Research Center, Moffett Field, CA 94035, USA.

Introduction: Mars' atmosphere is carbon dioxide dominated with non-negligible amounts of water vapor and suspended dust particles. The atmospheric dust plays an important role in the heating and cooling of the planet through absorption and emission of radiation. Small dust particles can potentially be carried to great altitudes and affect the temperatures there. Water vapor condensing onto the dust grains can affect the radiative properties of both, as well as their vertical extent. The condensation of water onto a dust grain will change the grain's fall speed and diminish the possibility of dust obtaining high altitudes. In this capacity, water becomes a controlling agent with regard to the vertical distribution of dust. Similarly, the atmosphere's water vapor holding capacity is affected by the amount of dust in the atmosphere. Dust is an excellent green house catalyst; it raises the temperature of the atmosphere, and thus, its water vapor holding capacity. There is, therefore, a potentially significant interplay between the Martian dust and water cycles.

Previous research done using global, 3-D computer modeling to better understand the Martian atmosphere treat the dust and the water cycles as two separate and independent processes [1]. The existing Ames numerical model will be employed to simulate the relationship between the Martian dust and water cycles by actually coupling the two cycles. Water will condense onto the dust, allowing the particle's radiative characteristics, fall speeds, and as a result, their vertical distribution to change. Data obtained from the Viking, Mars Pathfinder, and especially the Mars Global Surveyor missions will be used to determine the accuracy of the model results.

General Circulation Model: The water and dust cycles in the model will be coupled by depositing supersaturated water vapor onto the dust grains to form ice clouds. By using the dust as seeds for cloud formation, the radiative properties, fall speeds and vertical distributions of both will be altered [2,3,4]. Water ice encapsulating the dust grains makes the dust much less effective at the 15 μ m absorption band, but increases their potential as infrared scatterers [4]. Mie scattering (the scattering of light by a particle whose size is comparable to the wavelength of light) becomes important with the formation of cloud particles a few microns in size. The effectiveness of Mie scattering is large when

the size parameter is $2\pi r/\lambda \geq 1$, where r is the radius of the particle and λ is the wavelength of light.

The addition of water mass to these dust grains influences the gravitational sedimentation speed. Initially, the increase in mass decreases the sedimentation speed, and then the fall speed rapidly increases once the particle has doubled in radius, removing dust more quickly from the atmosphere [5]. The vertical extent of the dust will be at the mercy of the cloud deck. Little, if any, dust will be able to be transported past the saturation layer. Here, the dust will be used for seeds in cloud formation, effectively capping its altitude. The "snowing out" of these particles will move water out of the saturated layer to lower vertical levels as well.

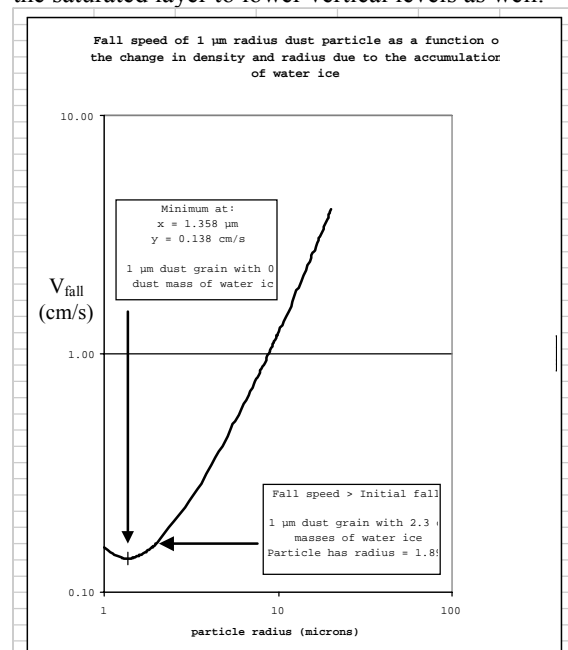


Figure 1. Fall speed vs. particle radius for a 1 μ m dust grain accumulating water ice. Initially, fall speed decreases since the decrease in density is the dominating factor. This trend is quickly reversed, as size (radius) of the particle becomes more dominant. The formulation of this curve is based on that found in [5].

Sublimation of ground ice is based upon the flux rate equations of Haberle and Jakosky [6] for buoyant diffusion (E_b) and turbulent mixing (E_t). These two processes are as follows:

$$E_b = (0.17)(\delta\eta)\rho D[(\delta\rho/\rho)(g/v^2)]^{1/3}$$

and

$$E_t = (0.002)\rho w q_s(1 - r)$$

where $\delta\eta$ is the difference between the surface concentration (by mass) of water vapor and that of the gas away from the surface, ρ is the density of the atmosphere, D is the diffusion coefficient of water vapor in CO_2 , g is the acceleration due to gravity, ν is the kinematic viscosity of CO_2 , $\delta\rho$ is the difference between the density of the atmosphere at the surface and the density of water vapor at the surface, w is the wind speed at the surface layer, q_s is the saturation mixing ratio of water vapor at the temperature of the ice, and r is the relative humidity [6].

The model will contain an adsorbing regolith based on the scheme developed by Houben et al. [7]. Water will be mobilized in an approximately 10 cm thick ground layer. The total adsorbed water capacity is by:

$$\alpha = \epsilon \rho_s [\beta P_{\text{H}_2\text{O}}^{0.51} / \exp(\delta/T)]$$

where ρ_s is the density of the regolith, β is the specific soil surface area for basalt, $\delta = -2679.8$ K, T is the temperature, $P_{\text{H}_2\text{O}}$ is the water vapor pressure in Pascals, and ϵ is a dimensionless parameter introduced to allow for scaling the adsorptive properties of other minerals. Increasing the value of ϵ will increase the adsorptivity of the soil, meaning the regolith can hold more water per unit volume [7].

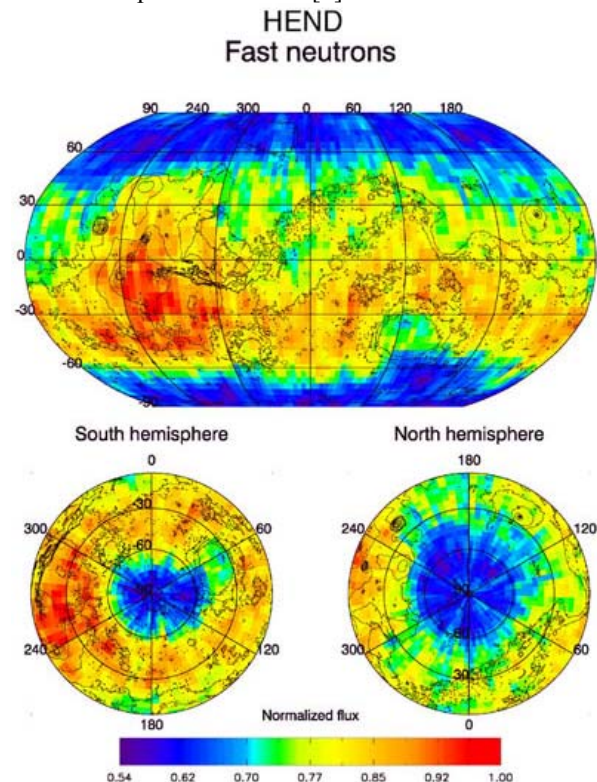


Figure 2. Initial map of fast neutrons by the High Energy Neutron Detector (HEND) on Mars Odyssey. Red areas are hydrogen-poor soil, while blue areas are hydrogen-rich. Note that Solis Planum (270°E, 30°S) is the most hydrogen-poor region on the planet. Hydrogen-rich areas extend from both poles to approximately 60° latitude, probably water ice buried beneath hydrogen-poor soil. Also, two smaller regions of hydrogen-rich soil occur in the equatorial zone, probably subsurface deposits of chemically and/or physically bound H_2O and OH . One is located at approximately 30° E and the other at 200° E longitude [8,10]. Figure by Mitrofanov et al. 2002.

The Mars Odyssey Orbiter is carrying a suite of instruments known as the Gamma Ray Spectrometer (GRS). The Martian water content in the top meter of soil can be determined independently by two instruments of the GRS suite [9]. A gamma ray spectrometer aboard GRS can directly measure the emission of hydrogen gamma rays. These gamma rays are detectable from the upper tens of centimeters in the surface [9]. A neutron spectrometer aboard GRS can indirectly sample hydrogen in the upper meter of the surface [9,10]. Since 99.985% of all hydrogen is in the form of ^1H (no neutrons), then hydrogen is detected by its characteristic lack of neutron production by cosmic rays. Comparison of these two independent results will allow a determination of the water distribution as a function of surface depth (maximum depth of ~1 meter) [9,10].

The current model will have an active regolith of only ~10 cm deep. GRS will help to constrain this model regolith since the GRS can obtain a vertical distribution for the adsorbed water of ~1 m, which is greater than that included into the model (~10 cm). Odyssey data will be used to tune the important parameter of water distribution in the upper one meter of the regolith.

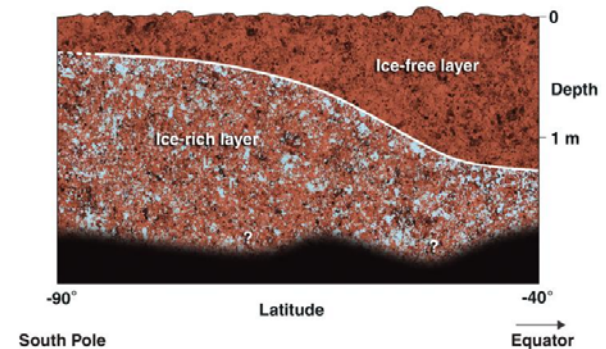


Figure 3. The Gamma Ray Spectrometer can determine the vertical distribution of ground water ice down to ~1 meter in depth. The above diagram is one possible configuration for water ice in the Martian regolith. Initial measurements suggest that the topmost layer of regolith is relatively ice-free. While a few tens of centimeters down, the regolith is 20 to 50 percent water ice by mass [11].

Figure taken from the web page of http://www.jpl.nasa.gov/images/mars/pia3803_caption.html

Discussion: TES and MAWD data will be looked at extensively to tune the model. Both TES and MAWD data will be used to help identify other possible sources and sinks of water vapor besides the north polar cap. TES will also be influential in identifying sources of dust storm activity by direct observation of where they begin, as well as finding possible sinks by identifying changes in surface albedo as a result of dust storm activity. GRS will be used to identify heterogeneity in the regolith, which previous models described homogeneously [1,7].

Smith (2001) compares the TES and MAWD data sets for the water vapor column abundance and finds three key differences [12]. At low northern latitudes between $L_s = 150^\circ$ and 205° , TES retrieves water vapor abundances 20-40% higher than that of MAWD. TES sees a gradual increase in water vapor abundance between $L_s = 40^\circ$ and 90° at mid-northern latitudes, where as MAWD sees an abrupt increase between $L_s = 60^\circ$ and 75° . Finally, excluding the dusty period of $L_s = 205^\circ$ - 330° seen by MAWD, TES derives a globally averaged amount of water vapor 10-20% higher than that seen by MAWD. These three differences are all within the error bars of the two instruments, but may be explained by interannual variability [12]. Coupling of the dust and water cycles in the model and running a multiyear simulation may help to disentangle the reason behind the differences in the TES and MAWD data sets.

The objective of this project is to determine the role the water cycle plays in interannual variability of the Martian atmosphere when coupled with the dust cycle. A possible consequence of the decoupling of the two cycles is that previous long duration models show no yearly variations. The patterns of dust lifting and sedimentation remain the same throughout multiple-year runs [13].

We are currently implementing the above mentioned water physics into the latest version of the Ames GCM. We will run the full 3-D model with just a polar source to be used as a base comparison. Subsequently, a multiyear run with an active regolith based on initial Mars Odyssey findings will be performed.

Acknowledgements: This work is being supported by NASA's Planetary Atmospheres Program (NASA/NAG5-1213) and also by the New Mexico Space Grant Consortium.

References: [1] Richardson R. I. and Wilson R. J. (2002) *JGR*, 107, 7-1-7-31. [2] Rodin A. V. et al. (1999) *Advances in Space Science*, 23, 1577-1585. [3] Clancy R. T. et al. (1996) *Icarus*, 122, 36-62. [4] Clancy R. T. et al. (1998) *AAS, DPS meeting #30*, Ab-

stract #09.02. [5] Murphy et al. (1990) *JGR*, 95, 14629-14648. [6] Haberle R.M. and Jakosky B.M. (1990) *JGR*, 95, 1423-1437. [7] Houben H. et al. (1997) *JGR*, 102, 9069-9083. [8] Mitrofanov I. et al. (2002) *Science*, 297, 78-81. [9] Boyton W. V. et al. (2002) *Science*, 297, 81-85. [10] Feldman W. C. et al. (2002) *Science*, 297, 75-78. [11] http://www.jpl.nasa.gov/images/mars/pia3803_caption.html [12] Smith M. D. (2002) *JGR*, 107, 25-1. [13] Murphy J. R. (1999) *5th International Conference on Mars*, Abstract #6087.

CHARACTERISTICS OF MINI-MAGNETOSPHERES FORMED BY PALEO-MAGNETIC FIELDS OF MARS. N. F. Ness¹, A. M. Krymskii², D. H. Crider³, T. K. Breus⁴, M. H. Acuna⁵, D. Hinson⁶ and K. K. Barashyan², ¹Bartol Research Institute, 104 Center Mall, #217, University of Delaware, Newark, DE 19716 USA, nfness@udel.edu, ²Rostov State University, Rostov-on-Don, Russia, ³The Catholic University of America, Washington, DC, ⁴Space Research Institute (IKI), Moscow, Russia, ⁵NASA-Goddard Space Flight Center, Greenbelt, MD, USA, ⁶Center for Radar Astronomy, Stanford University, Stanford, CA, USA.

Introduction: The intensely and non-uniformly magnetized crustal sources generate an effective large-scale magnetic field. In the Southern hemisphere the strongest crustal fields lead to the formation of large-scale mini-magnetospheres. In the Northern hemisphere, the crustal fields are rather weak and there are only isolated mini-magnetospheres. Re-connection with the interplanetary magnetic field (IMF) occurs in many localized regions. This may occur not only in cusp-like structures above nearly vertical field anomalies but also in halos extending several hundreds of kilometers from these sources. Re-connection will permit solar wind (SW) and more energetic particles to precipitate into and heat the neutral atmosphere. Electron density profiles of the ionosphere of Mars derived from radio occultation data obtained by the Radio Science Mars Global Surveyor (MGS) experiment are concentrated in the near polar regions. The effective scale-height of the neutral atmosphere density in the vicinity of the ionization peak has been derived for each of the profiles studied. The effective scale-heights have been compared with the crustal magnetic fields measured by the MGS Magnetometer/Electron Reflectometer (MAG/ER) experiment. A significant difference between the large-scale mini-magnetospheres and regions outside of them has been found. The neutral atmosphere is cooler inside the large-scale mini-magnetospheres. It appears that outside of the cusps the strong crustal magnetic fields prevent additional heating of the neutral atmosphere by direct interaction of the SW. The scale-height of the neutral atmosphere density derived from the experiment with the MGS Accelerometer has been compared with MAG/ER data. The scale-height was found to be usually larger than mean value near the boundaries of potential mini-magnetospheres and around “cusps”. It may indicate that the paleo-magnetic/IMF field re-connection is characteristic of the mini-magnetospheres at Mars.

POLAR DUNES RESOLVED BY THE MARS ORBITER LASER ALTIMETER GRIDDED TOPOGRAPHY AND PULSE WIDTHS. Gregory A. Neumann^{1,2}, ¹*Department of Earth, Atmospheric and Planetary Sciences, Massachusetts Institute of Technology, Building 54, 77 Massachusetts Avenue, Cambridge, MA 02139-4307, (neumann@tharsis.gsfc.nasa.gov)*, ²*Laboratory for Terrestrial Physics, Code 920, NASA/Goddard Space Flight Center, Greenbelt, MD 20771.*

The Mars Orbiter Laser Altimeter (MOLA) polar data have been refined to the extent that many features poorly imaged by Viking Orbiters are now resolved in densely gridded altimetry. Individual linear polar dunes with spacings of 0.5 km or more can be seen as well as sparsely distributed and partially mantled dunes. The refined altimetry will enable measurements of the extent and possibly volume of the north polar ergs.

MOLA pulse widths have been recalibrated using inflight data [2], and a robust algorithm applied to solve for the surface optical impulse response. Figure 1 shows the surface root-mean-square (RMS) roughness at the 75-m-diameter MOLA footprint scale, together with a geological map [4]. While the roughness is of vital interest for landing site safety studies, a variety of geomorphological studies may also be performed. Pulse widths corrected for regional slope clearly delineate the extent of the polar dunes.

The MOLA PEDR profile data have now been re-released in their entirety (Version L). The final Mission Experiment Gridded Data Records (MEGDR's) are now provided at up to 128 pixels per degree globally. Densities as high as 512 pixels per degree are available in a polar stereographic projection. A large computational effort has been expended in improving the accuracy of the MOLA altimetry themselves, both in improved orbital modeling and in after-the-fact adjustment of tracks to

improve their registration at crossovers [1]. The current release adopts the IAU2000 rotation model and cartographic frame [3] recommended by the Mars Cartography Working Group. Adoption of the current standard will allow registration of images and profiles globally with an uncertainty of < 100 m.

The MOLA detector is still operational and is currently collecting radiometric data at 1064 nm. Seasonal images of the reflectivity of the polar caps can be generated with a resolution of about 300 m per pixel.

References

- [1] Neumann, G. A. et al., *J. Geophys. Res.*, 106, 23,753–23,768, 2001.
- [2] Neumann, G. A. et al., *Geophys. Res. Lett.*, in press, 2003.
- [3] Seidelmann, P. K., et al., *Cel. Mech. Dyn. Astron.*, 82, 83–110, 2002.
- [4] Tanaka, K. L., and D. H. Scott, Geologic map of the polar regions of mars, scale 1:15,000,000, 1987.

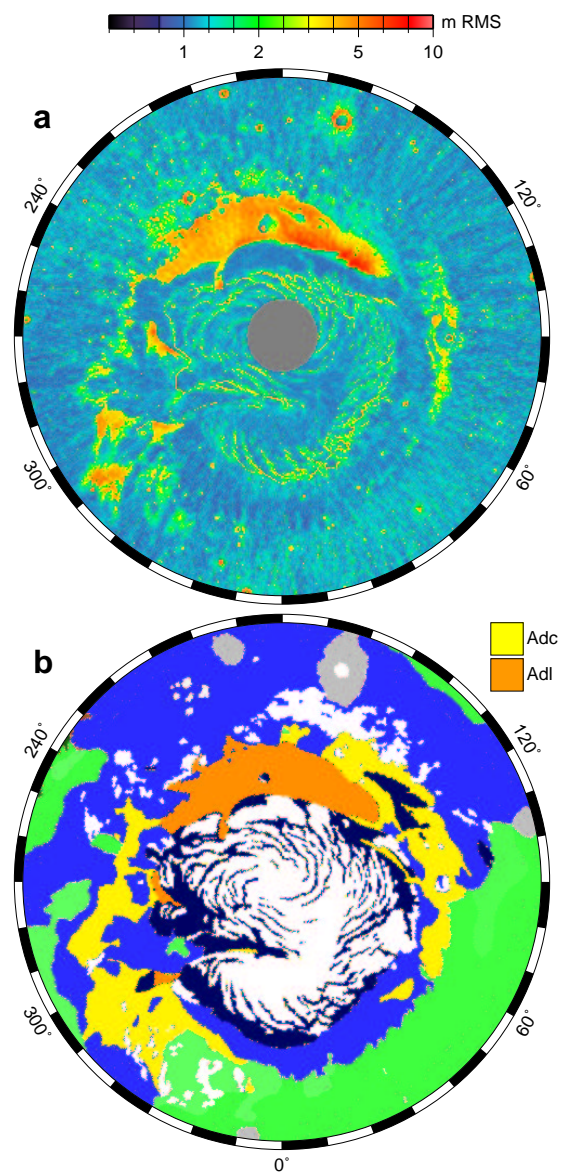


Figure 1: (a) North polar RMS roughness and (b) geological map, in polar stereographic projection.

FLUVIAL AND LACUSTRINE PROCESSES IN MERIDIANI PLANUM AND THE ORIGIN OF THE HEMATITE BY AQUEOUS ALTERATION. H. E. Newsom¹, C. A. Barber¹, R. T. Schelble², T. M. Hare³, W. C. Feldman⁴, V. Sutherland¹, A. Livingston⁵, and K. Lewis⁵, ¹University of New Mexico, Institute of Meteoritics and Dept. of Earth and Planetary Sciences, Albuquerque, NM 87131, newsom@unm.edu, ²Dept. of Earth Sci., Univ. of Southern California, Los Angeles, CA 90089, ³U.S. Geol. Survey, Flagstaff, AZ, 86001, ⁴Los Alamos National Laboratory, Los Alamos NM 87545, ⁵Southwestern Indian Polytechnic Institute, Albuquerque, NM 87184.

Introduction: The prime MER landing site in Meridiani Planum is located on layered materials, including hematite, whose origin as lacustrine or aeolian sediments, or volcanic materials is uncertain. Our detailed mapping of the region provides important constraints on the history of the region. Our mapping of the location of fluvial and lacustrine land forms in the region relative to the layered deposits provides new evidence of a long history of erosion and deposition as has long been noted [1]. In addition, our detailed mapping of the southern boundary of the hematite deposit strongly supports an association between long-lived fluvial channels and lacustrine basins and the strongest hematite signatures. This evidence supports an origin of the hematite deposits by interaction with water under ambient conditions in contrast to suggestions of hydrothermal processes due to volcanic or impact crater processes. An important part of the story is the evidence for the localization of the layered deposits due to topographic control induce by the presence of a large early basin we have identified that extends to the north-east of the landing site.

Distribution of current channel networks, drainages, and basins

Channel systems leading to the southern boundary of the hematite-rich surface deposit can be observed originating from a large highlands region that extends south-eastwards from the hematite regions for hundreds of kilometers (Fig. 1, inset). These channels appear to terminate near the boundary with the hematite deposit. Based on the Viking data, Edgett and Parker [1] identified this boundary as the edge of an ocean or large body of water. However, careful examination of the high resolution MOC images and the MOLA topography clearly shows that these highly visible channels flowed into a system of paleo-lakes and channels that currently appear to drain westward into the unnamed 150 km diameter crater, and further east towards Iani Chaos. A possible extension of the drainage area to the south of Schiaparelli basin includes Evros Vallis. Because the topography is so flat in the area between the two drainages, the topographic gradient cannot be easily determined, and may have varied in direction at different times in the past. The total area of the drainage region is impressive, 580,000 km², about the size of the state of Texas. The area for the northwestern portion of the drainage area closest to the hematite area is 200,000 km², about the size of

Kansas. The area for the Evros Vallis portion is 380,000 km². There is also a large system of highland valleys (not mapped in this study) that fed into the lowland region east of the hematite area. If flooded, this lowland would currently drain to the north.

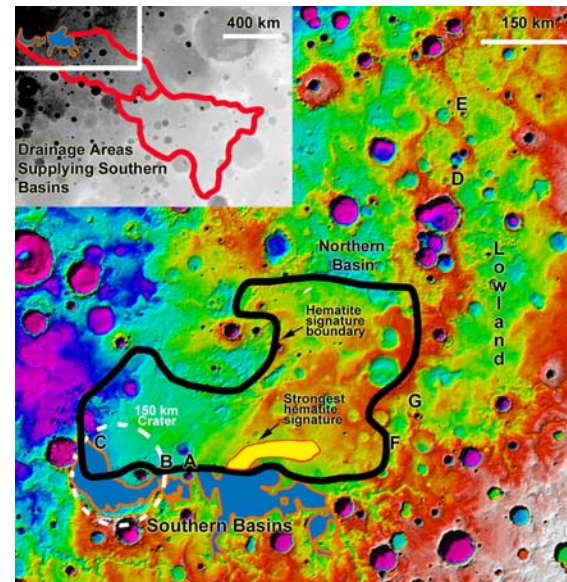


Fig. 1 Study area in Meridiani Planum. MOLA topography map (Latitude 7 N to 5.6 S, Longitude 351.1 E to 5.5 E) showing the regional setting of the hematite-rich surface deposit labeled with areas and basin barriers [1]. The inset shows the drainage areas feeding the southern basins.

Fluvial and lacustrine environments along the southern boundary of the hematite deposit are currently constrained by topographic barriers that serve to define three linked basins, including the southern part of the 150 km crater (Fig. 3, a-d, Fig. 4, a). These basins are progressively lower from east to west, and evidence exists for fluid flow through channels that have partially breached the barriers.

The western basin is located within the 150 km diameter crater, where a channel leads south around the lobe of hematite-rich material that covers the northern portion of the crater. High-resolution images of the floor of the channel (Figs. 3 a-c) show characteristic evidence of fluvial erosion of ancient cratered terrain, very similar to images from the Gusev crater (e.g. Fig. 5). Evidence of recent fluid flow in this system of basins may include the erosion of ejecta blanket material from a 21 km diameter crater superimposed on the

FLUVIAL AND LACUSTRINE FEATURES IN MERIDIANI PLANUM H. E. Newsom, et al.

hematite deposit (Fig. 4a). The western basin is constrained by a barrier (C, Lat. 2.09 S, Long. 352.22 E), at an elevation of -1760 m where a channel leads to a smaller crater (19 km diameter) superimposed on the rim of the 150 km diameter crater. The area of the western basin is approximately 9,000 km², with an average depth of 40 m and a volume of 1100 km³.

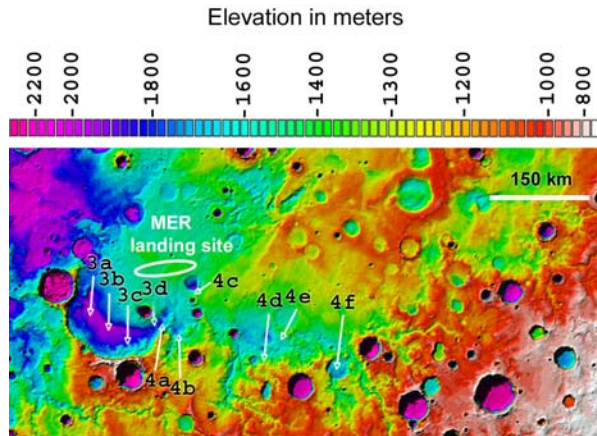


Fig. 2. Detail of the southern paleo-lake basins and channels in the study area. The locations of high-resolution images Figs. 3 and 4 are shown. Also shown is the approximate location of the prime “Hematite Site” landing ellipse for the 2003 MER mission.

The central basin of the three is constrained by a barrier (B, Fig. 1) at an elevation of -1620 m, originally formed by the rim of the 150 km diameter crater to the west. The current area of the central basin is somewhat less than 2000 km², with an average depth of 40 m and a volume of approximately 80 km³. At the point where several channels flow into this central basin from the south, evidence exists for possible shorelines and erosion, although exposure of layered deposits cannot be ruled out (Fig. 4b). The elevation of the putative shorelines is consistent with the elevation of the barrier (“B” Fig. 1) that constrains the height of this basin.

In the eastern basin, water flowing in from the south is constrained by a barrier (labeled A Fig. 1, Lat. 2.78 S, Long. 354.68 E) at -1450 m elevation that is partly formed by a relatively young crater (6 km diameter) and there is evidence from the formation of a channel eroded in the ejecta blanket for flow around the north of this crater (Fig. 4c). Evidence for possible shorelines or eroded layered deposits is seen in Figs. 4d, and 4e. The elevation of the area in 4e (-1495 m) is consistent with the elevation of the barrier “A” (Fig. 1) that constrains the elevation of this possible lake. Fig. 4f shows eroded deposits where a major channel enters the basin. The current area of the eastern basin

is about 20,000 km² with an average depth of about 100 m and a volume of approximately 2,000 km³. The current base level for this eastern lake may have been lower earlier in martian history. For example, channels entering this basin (Fig. 2) are present down to the -1615 m elevation, a level, more appropriate for the basin defined by the barrier down stream (B, Fig. 1, Lat. 2.80 S, Long. 354.12 E, -1623 m).

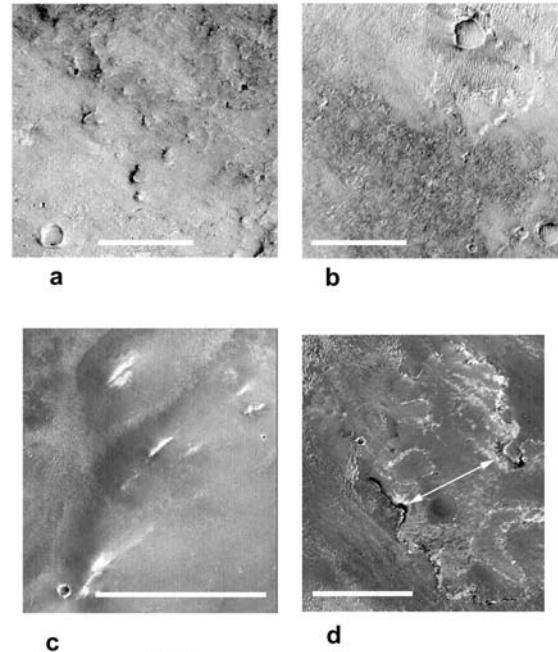


Fig. 3. a, b, c. MOC images of the channel floor on the bottom of the 150 km diameter crater. The ancient cratered surface exhibits evidence for fluvial erosion consistent with flow around the circumference of the floor of the crater. All scale bars are one kilometer in length (a, M1300898, b, M0300371; c M1301419). d. Part of the channel leading down into the 150 km diameter crater is shown with an arrow denoting the breadth of the channel (M0301632).

A broad lowland area is present along the eastern boundary of the hematite deposit. This lowland is approximately 80 km wide and extends for 450 kilometers to the north where it then heads back to the west. There are at least two areas where water in this lowland may have escaped to the west (D, Fig. 1, Lat. 6.60 N, Long. 1.60E, elevation -1220 m and E, Fig. 1, Lat. 4.94 N, Long. 1.97 E, elevation -1235 m). This eastern lowland has a heavily cratered topography with an extremely gentle gradient (≈ 30 m over 450 km, slope $<0.01\%$). This lowland area appears to be fed by channels from the vicinity of Schiaparelli basin and the older basin just to the south of Schiaparelli (not mapped). There is another basin area separating the eastern lowland area from the chain of basins along the southern boundary of the hematite. The western bar-

rier of this basin (F, Fig. 1, Lat. 2.66 S, Long. 359.22 E) is at an elevation of -1220 m, and the eastern barrier (G, Fig. 1, Lat. 0.94 S, Long. 0.47 E) is at an elevation of approximately -1260 m, and includes an impact crater (9 km diameter) that may have recently created a higher dam between the two drainages.

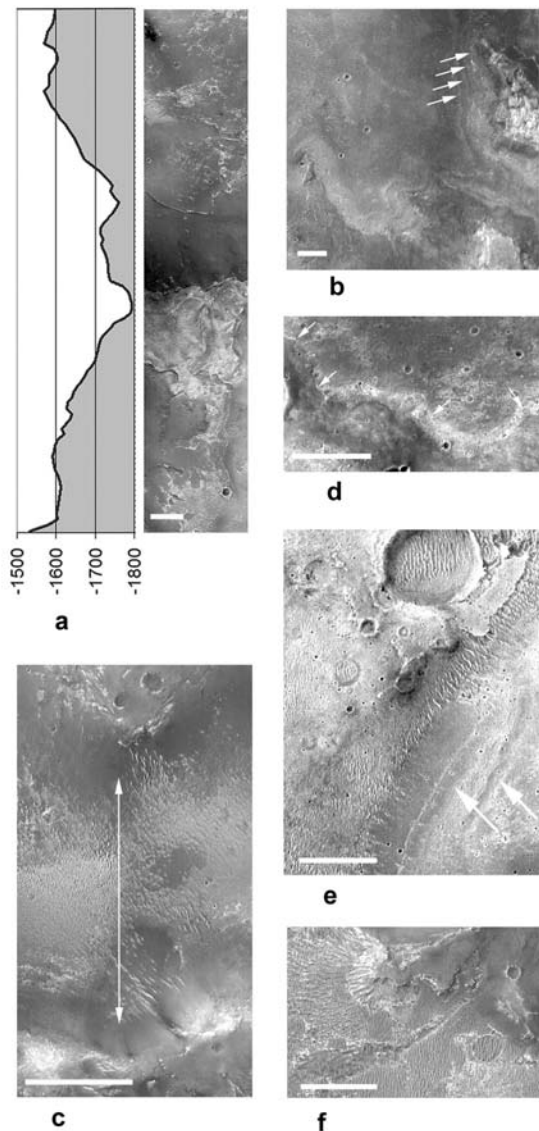


Fig. 4. Channel and basin features. All scale bars are one kilometer. a. An image of the channel leading into the 150 km diameter crater, just upslope of Fig. 3d, with the corresponding MOLA profile. The deeper channel has no apparent impact craters on the surface (M0201539, 2.94 km width). b. Possible shorelines in the central basin (mosaic of AB107704, M0901839). c. A channel eroded into ejecta deposits north of a relatively young crater that makes up part of barrier A (M1001349). The breadth of the channel is denoted with an arrow. d. Possible shorelines at approximately -1600 m on the south shore of the eastern basin

(M0204225). e. Possible shorelines in the eastern basin where an outlier of hematite fills the floor of a small basin (M1003047). f. Channels eroded on the floor of the eastern basin where a major channel enters the basin (M0700487).

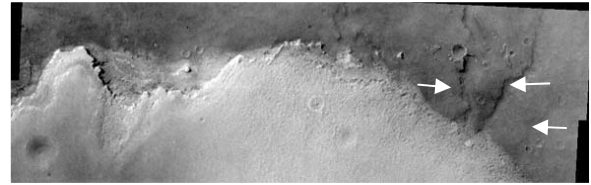


Fig. 5. Contact of layered material representing a hematite outlier with the floor of the northern basin in the center of the 800 km diameter impact structure (THEMIS visible image V03208003). Previously eroded channels (arrows) on the floor of the basin are being revealed by the erosion of the layered material. Image width is 30 km.

The northern boundary of the hematite deposit is characterized by a poorly integrated system of basins and channels that drains westward. This system of channels and depressions is not fed by a distinctive set of channels from higher elevations, but does represent a lower area surrounded by both the hematite deposit on the south, and cratered terrain to the north. The water in this system could have come from groundwater supplied from the paleo-lakes along the southern boundary and the eastern boundary of the hematite area since the elevations in the northern basin area just north of the hematite (Figs. 1, 5) are as low as -1700m and are generally lower than -1500 m.

History of the channel and lake systems

The geologic history of this region is complex and occurred over a time period extending to before 3.8 billion years. The hematite area occupies the southern half of an ancient basin or circular structure approximately 800 km in diameter (Fig. 6) [3]. This evidence includes a central basin, a 200 m high raised ring at a radius of 200 km (400 km diam.), and an annular trough at a maximum radius of about 400 km (800 km diam.). The western edge of the annular trough is missing, probably due to later erosion. The structure is very similar in size to the Cassini structure, which has a 400 km diameter rim and an 800 km diameter annular trough. The overall relief of the structure is currently very small (<500m), but there is strong evidence for extensive erosion, especially on the western side. The presence of a magnetic anomaly in the center of this structure suggests a very ancient age [4]. The presence of this structure probably controlled the deposition of the layered materials and the location of the fluvial channels and lacustrine basins in this area.

The formation of layered deposits of unknown composition throughout the Sinus Meridiani also oc-

FLUVIAL AND LACUSTRINE FEATURES IN MERIDIANI PLANUM H. E. Newsom, et al.

occurred early in Mars history [2]. The origin of these deposits is not clear, but may include basin ejecta, air-fall dust, volcanic, and sedimentary deposits. Edgett [5] has mapped the occurrence of dark mesa-forming units in 116 MOC images of craters throughout western Arabia Terra. All six occurrences of the dark mesa-forming units are located within the 800 km diameter feature, supporting the importance of this structure to the history of the area. These dark units are emplaced on previously eroded lighter material [6]

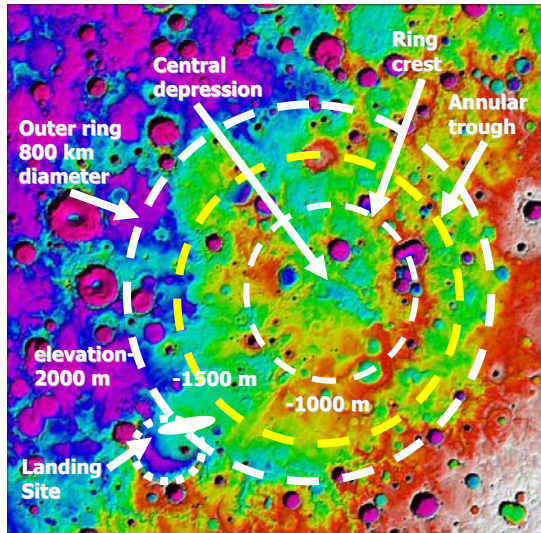


Fig. 6 Color coded MOLA topography showing concentric circular features in Meridiani Planum consistent with the presence of an 800 km diam. multi-ringed impact structure. The location of the MER landing site inside a 150 km diam. crater is also shown.

The formation of the current system of basins and fluvial channels in the region developed over a long period, with substantial resurfacing events extending into the Hesperian and chaos formation extending into the Amazonian and possibly into the very recent history [7]. The channel networks were periodically disrupted by cratering events that created or destroyed barriers. For example, at the present time the channels that extend into the eastern and central basins are incised to elevations well below the current elevation of the barriers (Fig. 2). This implies that earlier in martian history the barriers were at a lower base level before the late cratering events created new dams at higher elevations (e.g. barriers A, and G).

The origin of the smooth layered material as a lacustrine sedimentary deposit is difficult to explain as some of the areas containing the hematite signature are at an elevation (-1200 m) that is 150 m above the elevation of the present barrier constraining the large

eastern basin on the southern side of the hematite region. However, sedimentary deposition had to occur down stream from the very extensive areas eroded during channel formation in the drainage areas. The most likely candidate for a sedimentary deposit overlain by a hematite-rich surface is the lobe of material that fills the northern part of the 150 km diameter crater, and the area just to the north of the crater rim, which is at least partially dammed by several large craters (21 km, 19 km, and 31 km in diameter) now largely buried but still visible on the western edge of the area covered by the hematite deposits. Based on a thickness ranging from 200 m up to 500 m in the northern portion of the 150 km diameter crater, the volume of the partly layered material filling the crater is approximately $4,000 \text{ km}^3$. The estimated volume of deposits within the crater could be supplied by uniform erosion of a layer less than 4 m deep over the drainage area that possibly supplied water to the system.

Conclusions

The evidence for abundant fluvial and lacustrine activity and the discovery of the 800 km diameter structure provides a link between the Meridiani and Aram basin (500 km diameter) occurrences of hematite [8]. Both deposits share the combination of location on an elevated region within a large impact feature combined with a long history of fluvial and lacustrine activity suggesting that the hematite formed by a process involving the presence of water during wetter periods of martian history [9]. The MER rover may be able to provide evidence for the involvement of water with the formation of the hematite in terms of both rock studies and evidence for fluvial activity. The rover may also be able to determine the sedimentary vs. volcanic origin of the deposits.

References: [1] Edgett and Parker, *GRL* 24 2897, 1997 [2] Edgett and Malin 2000, *Science*. 105, 1927-1937, 2000. [3] Newsom et al., (2003) *JGR*, submitted. [4] Acuna et al., *Science* 284, 790, 1999. [5] Edgett (2002) *J. Geophys. Res.*, 107(E6), doi:10.1029/2001JE001587. [6] Hynek and Phillips, (2002) *Geology* 29, 407. [7] Grant and Parker, *J. Geophys. Res.*, 107, 5066, doi: 10.1029/2001JE001678, 2002. [8] Christensen P.R., et al. (2001), *JGR* 106, 23,873. [9] Kirkland et al. (2002) *Lunar and Planetary Science XXXIII*, CD rom #1218.

Research supported by NASA Planetary Geology and Geophysics program NAG 5-8804, NAG 5-11496 and NASA OSS-MURED Partnership program NAG 5-10143.

FIRST PLANETARY ROCK CORING IN OUR SOLAR SYSTEM...ESA 2003 BEAGLE 2 MARS LANDER

T.C. Ng¹, K.L. Yung², C.H. Yu², and C.C. Chan³

¹Dentist (holinser@vol.net),

²The Hong Kong Polytechnic University (mfklyung@inet.polyu.edu.hk, icchyu@inet.polyu.edu.hk),

³SolidWorks Corporation (ccchan@solidworks.com.hk).

Introduction:

ESA is going to send Beagle 2 to Mars in 2003 for exobiology exploration. On board, there are 3 sampling tools on board as follows:

1/ ROCK CORER - able to retrieve powdered rock sample; 370 gm in mass; size of a cigarette pack; 2 watts energy consumption; able to drill/grip/core/grind; multi-operational; split drill-bits design for anti-jamming.

2/SCOOP - gripper able to open/close by pressure; able to retrieve surface soil sample; device designed in case the rock corer is not functioning; multi-operational.

3/ MOLE - able to retrieve subsurface soil at required depth; multi-operational.

All the sampling tools are able to deliver samples into GCMS for in-situ analysis.

For more information,
please visit <http://www.hkmars.net>

THE NATURE OF THE MARTIAN AQUEOUS ENVIRONMENTS RECORDED BY ALH84001 CARBONATES. P.B. Niles¹, L.A. Leshin^{1,2}, and Y. Guan¹, ¹Department of Geological Sciences, ²Center for Meteorite Studies, Arizona State University (Box 871404, Tempe, AZ 85287-1404); pniles@asu.edu

Introduction: Direct evidence for the existence of water on Mars consists of morphologic features, thermal spectroscopic signatures of hematite, detection of H₂O ice in the polar caps, neutron spectroscopy, and secondary minerals preserved in martian meteorites. The martian meteorites currently provide the best opportunity to assess the detailed nature of the aqueous environments that once existed on Mars, simply because of the high level of capability of Earth based analytical techniques.

The martian meteorite ALH84001 has a 4.5 Ga crystallization age and it contains a unique assemblage of secondary carbonates that formed on Mars 3.9 Ga [1]. The meteorite is remarkably well preserved but has been extensively shocked. This provides an opportunity to learn specific environmental constraints of the nature of one or more aqueous systems on early Mars.

The meteorite shows very little evidence for aqueous weathering. Olivine, maskelynite, and orthopyroxene are all unaltered despite their vulnerability to aqueous alteration [2]. Secondary silica and pyrite have been reported [3], although there are virtually no clay minerals present. Given the highly fractured and shocked nature of this rock, the lack of aqueous alteration is a significant constraint on its aqueous history.

The chemical compositions of the carbonates preserved in the meteorite occupy a very well defined trend on a ternary plot (Fig. 1). Petrographic relationships suggest that the first carbonates to form were Ca-rich and that later forming carbonates became increasingly Mg-rich. The last phase to form was nearly pure magnesite. This sequence of carbonates commonly occurs as "rosettes" which have Ca-rich cores grading to Mg-rich rims.

The oxygen isotopic compositions of the carbonates have been well documented in a number of studies [4-7]. The ion microprobe data has proven to be extremely useful by being able to tie microscale isotopic measurements to precise chemical compositions, and petrographic location. All of the published ion microprobe data show identical relationship with chemical and isotopic composition. The isotopic data lie within a broad trend of increasing $\delta^{18}\text{O}$ values with increasing Mg content. The $\delta^{18}\text{O}$ values range from $\sim 0\text{‰}$ to $\sim 26\text{‰}$ (SMOW) over distances of only 100's of microns.

Knowledge regarding the nature of the aqueous system(s) that formed these carbonates will be very useful in answering long held questions regarding the history of water on Mars. Unfortunately, despite numerous studies, the nature of the aqueous system(s) that formed the ALH84001 carbonates is still heavily disputed. Some studies have favored an aqueous system at low temperatures ($<100^\circ\text{C}$) [4, 8], others favored a high temperature ($>150^\circ$) low fluid/rock system [9, 10], while still others have argued for an aqueous environment heavily influenced by biological activity [11].

The high temperature ($>150^\circ\text{C}$) models typically call for small amounts of very CO₂ rich fluids which are injected into the rock on very short timescales [9]. The nature of the CO₂ fluids range from melted carbonate to water super-saturated with CO₂. The major problem with the high temperature models is the lack of alteration in the olivine, pyroxene, and maskelynite. However, these models argue that the CO₂ rich nature of the fluid combined with the short duration would preclude any weathering [9].

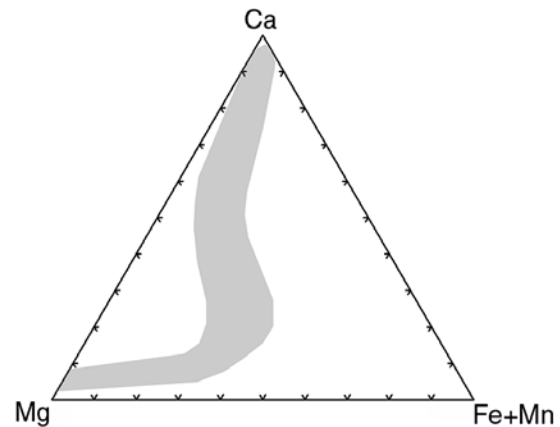


Figure 1. The gray area shows the range of chemical compositions of ALH84001 carbonates. Carbonates outside of this range are very rare.

Low temperature ($<100^\circ\text{C}$) models call for the carbonates to be precipitated in an aqueous event with a higher fluid/rock ratio and a somewhat longer duration. Two studies have argued for an evaporative aqueous event that explains the changes in both the chemical and the isotopic compositions [12, 13]. These models are all based on the lack of equilibrium

relationships in chemical or isotopic compositions and the lack of evidence for chemical weathering [4].

The biological models have argued that the carbonates formed in a low temperature (<100°C) environment and the precipitation of the carbonates was heavily influenced by biological factors [11].

It is clear that further constraints are needed in order to determine the nature of the aqueous system that formed the ALH84001 carbonates. All of the existing evidence can be used to support either a high temperature or low temperature system.

This study sets out to begin to provide additional constraints from new ion microprobe carbon isotopic measurements of the carbonates. The carbon isotopic composition of the carbonates will provide a second independent data set that can be used as a powerful constraint in evaluating existing models for the formation of the ALH84001 carbonates and formulating new ones.

Analytical Methods: Samples were prepared in a manner that minimized contamination of the carbonates with other carbon bearing materials such as epoxy, hardeners, or polishing materials. Two small chips of ALH84001 were encased in epoxy, and then polished to expose a carbonate bearing surface. Epoxy penetration was observed to be limited to the large fractures near the edges of the chip. Polishing was accomplished using silica carbide coarse grit sandpaper initially, followed by alumina paste. The samples were ultrasonically cleaned in distilled water in between each grit step.

Carbonate grains were characterized using a JEOL 8600 electron microprobe with a WDS detector system at Arizona State University. Ion microprobe analyses were performed on the IMS 6f at Arizona State University. Measurements were collected using two different analytical techniques during four separate sessions. The two analytical techniques are extreme energy filtering (EEF) and high mass resolution (HMR).

During sessions where extreme energy filtering was used a 3.9 nA Cs⁺ beam was focused to a spot size of ~30 nm diameter using critical illumination. Secondary ions were collected at -9 kV with an offset of 325 V as in Hervig [14]. Typical count rates on ALH carbonates were ~4*10⁴ cps for ¹²C.

In sessions using the high mass resolution (HMR) technique, a 0.4 nA Cs⁺ beam was focused to a spot size of ~10 nm using critical illumination. Secondary ions were collected at -9 kV with no energy offset. Typical count rates on ALH carbonates were ~4*10⁵ cps for ¹²C.

For all analytical sessions instrumental mass fractionation (IMF) was calculated using analyses of carbonate standards mounted in the same slide as the me-

teorite. The standards used consist of calcite, dolomite, magnesite and siderite. For all of the analytical sessions, IMF was calculated using a linear interpolation between the values measured for dolomite, siderite and magnesite. The lack of correlation of IMF with any known parameter such as chemical content, analysis conditions, or secondary yield force us to use an approximation using linear relationships (Leshin et al., 1998). The agreement of the two data sets using entirely different analysis conditions and IMF corrections suggests that the uncertainty for the IMF correction is accurate to within the calculated uncertainty.

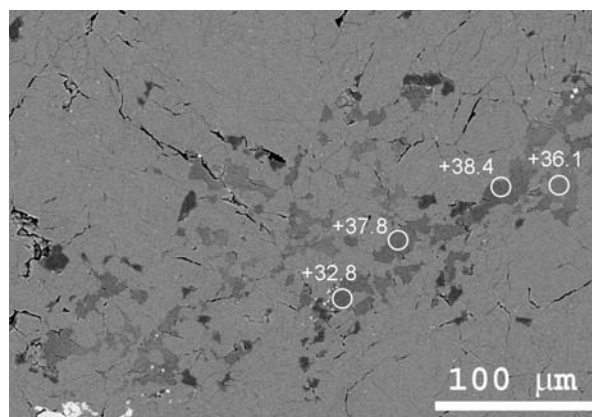


Figure 2. SEM backscatter image of the location of some of the analyses in this study. The numbers show the $\delta^{13}\text{C}$ values (PDB) measured for each spot.

Results: The $\delta^{13}\text{C}$ of the ALH84001 carbonates range from 27‰ to 64‰ relative to PDB (Fig. 3). These results firmly establish $\delta^{13}\text{C}$ variability in ALH84001 carbonates and considerably expand the range of values obtained by conventional techniques. The data show a general correlation between $\delta^{13}\text{C}$ and mole fraction of magnesium, with the most magnesian carbonates having the highest $\delta^{13}\text{C}$ values. This result is also consistent with previous bulk analyses [8, 15]. The amount of scatter in the data is comparable to the scatter in the ion microprobe oxygen isotope data for ALH84001 carbonates, and consistent with estimates of uncertainties.

The range of compositions of carbonates analyzed range from magnesite to Ca-poor ankerite. The data do not include analyses of more calcium rich carbonates due to their rarity in the available polished thick sections. No complete rosettes were available for analysis, so almost all the carbonates analyzed were patchy in nature (Fig. 2).

Discussion: The ~30‰ range of carbon isotopic values measured in the ALH84001 carbonates has no terrestrial analog. Variations of similar magnitude have been found in the same localities but never in the

same rock on the scale of millimeters. Combined with the variations of the chemical and oxygen isotopic compositions, the carbon isotopic data are difficult to reconcile with current formation models.

High temperature (>150°C) models require a closed system, low fluid/rock model to explain the oxygen isotopic data. However this model is inconsistent with the large carbon isotopic variations observed. One cannot create a 30‰ variation in carbon isotopic composition using a Rayleigh distillation caused by progressive carbonate precipitation as proposed by Leshin et al. [6].

Low temperature (<150°C) models run into similar difficulties. Most low temperature models use temperature change to explain the oxygen isotopic variations. Some low temperature models use evaporation to explain the oxygen isotopic compositions. Both of these cases cannot explain the carbon isotopic compositions. A temperature change from 300°C to 0°C would be needed in order to explain the carbon isotopic variation under equilibrium conditions [16]. Evaporation would not be able to create the observed variation in carbon isotopic composition without very high salinities [17]. However, at high salinities evaporation would not be able to produce the oxygen isotopic variation [18].

Biological models for the formation of the carbonates are not specific enough to test in this manner. Large carbon isotopic variations in carbonates on Earth are frequently attributed to mixing between organic and inorganic reservoirs [19]. This could be possible in the ALH84001 carbonates with the earliest Ca-rich carbonates incorporating organic carbon and the later Mg-rich carbonates incorporating mainly inorganic carbon. However, the association of the magnetite “bio-minerals” with the magnesite rims which have the heaviest carbon isotopic compositions makes this possibility seem less likely.

$\delta^{13}\text{C}$ vs. X_{Mg} ALH84001 Carbonates

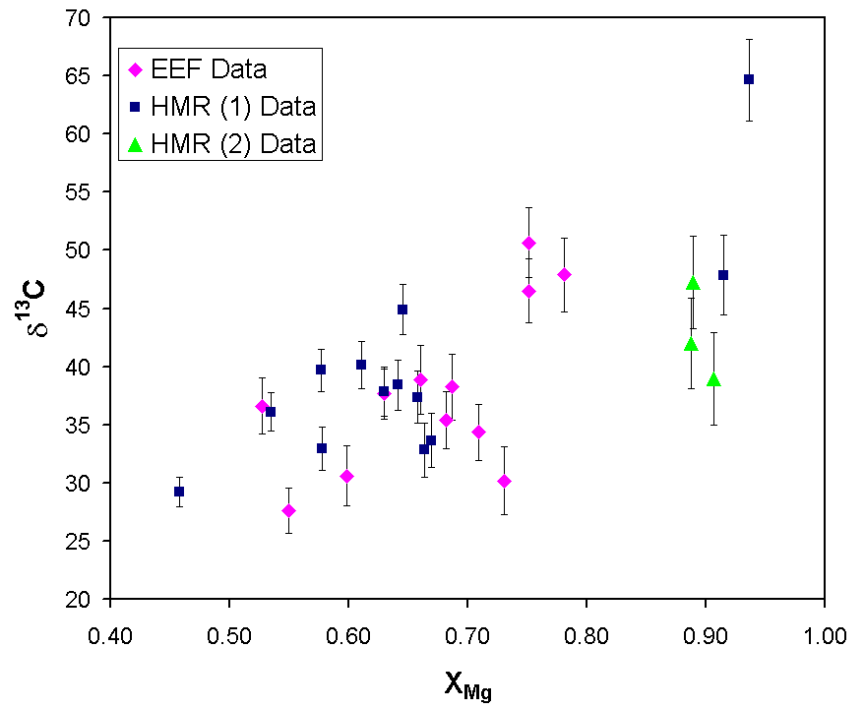


Figure 3. Carbon isotopic compositions of carbonates in ALH84001 as measured by ion microprobe. The carbon isotopic composition is plotted against mole fraction of magnesium measured by electron microprobe. Uncertainties shown include counting statistics within a each measurement and the point to point reproducibility of the instrument.

We propose three new models that provide potential geologically reasonable environments that satisfy constraints from the chemical, isotopic, and petrographic data collected thus far: Mixing between two distinct fluids, CO_2 rich spring environment, and a CO_2 rich spring environment.

Mixing Model: The most common way of interpreting covariant carbon and oxygen isotopic trends on Earth is through a mixing process between marine and meteoric waters [19]. However, these trends are typically measured using samples from different stratigraphic depths, or entirely different outcrops. The trends observed in the ALH84001 carbonates are present on the scale of microns in one sample. The differences in scale make it difficult to compare to terrestrial examples because there is very little data for large isotopic variations on a micro-scale. Mixing models that are typically applied to interpret terrestrial carbonate localities may not be applicable to the micro-scale. Nevertheless a mixing model does provide a possible way to explain much of the data and observations made on the meteorite.

Carbonates are precipitated, in this scenario, during the mixing of two chemically and isotopically distinct

fluids at a constant temperature. The variations observed in the carbonates are a result of different proportions of the two end member fluids. It has been interpreted, based on petrographic relationships, that the more calcium rich carbonates formed first, followed by a steady progression of more magnesium and iron rich carbonates [6]. Among the final carbonates to form in this interpretation are the magnesite rims. Thus, the initial carbonates, in this model, are precipitated by a relatively calcium rich fluid which is isotopically light in both oxygen and dissolved CO₂. The progression in chemical and isotopic compositions begins with the addition of small amounts of the second fluid which is magnesium rich and isotopically heavy in both $\delta^{18}\text{O}_{\text{H}_2\text{O}}$ and $\delta^{13}\text{C}_{\text{CO}_2(\text{aq})}$. In the final stages of precipitation the system is dominated by the second fluid which is precipitating isotopically enriched magnesite.

CO₂ rich Spring: Temperature change and CO₂ degassing are two mechanisms that frequently occur in terrestrial spring environments where warm (<80°C) CO₂ rich water is emitted from the ground [20-22]. In this model, small amounts of CO₂ rich warm water are directly injected into the proto-meteorite ALH84001. This fluid undergoes cooling and extensive CO₂ degassing: the combined effects of which can explain the oxygen isotopic, carbon isotopic, and chemical compositions of the carbonates.

The carbon and oxygen isotopic compositions of the carbonates undergo progressive enrichment due to the linked processes of cooling and CO₂ degassing. A simple equilibrium temperature change from 80°C to 0°C can cause $\delta^{18}\text{O}$ enrichment in carbonates of ~+20‰ [6, 7]. The temperature change also causes an equilibrium enrichment of ~8‰ in $\delta^{13}\text{C}$ [16]. Additional enrichment of $\delta^{13}\text{C}$ occurs during extensive CO₂ degassing which causes a kinetic isotope effect that can conceivably cause a ~+25‰ enrichment in $\delta^{13}\text{C}$ through degassing of 80% of the CO₂ from solution [21].

High pH Spring: High pH fluids provide a means to create large variations in the carbon and oxygen isotopic compositions of carbonates precipitated in spring environments. This occurs through a kinetic process as CO₂ rapidly invades the high pH, CO₂ free water emerging from the ground. Carbonates with similar carbon and oxygen isotopic variations have been discovered in high pH spring environments in Oman [23]. The variation in the chemical compositions of the carbonates is also consistent with this type of environment [24].

These springs are excellent analogs for ancient Mars. High pH fluids form as a consequence of ser-

pentization which occurs at high or low temperatures. This would likely be common on the early Martian surface which was probably dominated by ultra mafic rocks similar to ALH84001. If water-rock interactions occurred on early Mars as postulated by many studies (e.g. [25]), then one would expect the fluids to be high pH in character.

Conclusions: (1) The ALH84001 carbonates show a minimum of a 35‰ variation in $\delta^{13}\text{C}$ that is correlated with the chemical composition and petrographic relationships of the carbonates. The early forming Ca rich carbonates have the lowest $\delta^{13}\text{C}$ values, while the late forming Mg rich carbonates have the highest $\delta^{13}\text{C}$ values.

(2) The large range in the carbon isotopic compositions of the ALH84001 carbonates is not consistent with their formation from limited amounts of CO₂ rich fluid where isotopic variation is caused by a Rayleigh distillation process.

(3) The isotopic composition of the carbonates is not consistent with their formation from an evaporative environment, or a simple low temperature environment.

(4) The carbonates likely formed in three possible environments: mixing of fluids from different isotopic reservoirs, CO₂ rich spring environment, and a high pH spring environment.

References: [1] Borg, L.E., et al. (1999) *Science* **286** 90-94. [2] Wentworth, S.J. and J.L. Gooding, in *Lunar and Planetary Institute Conference Abstracts*, 1489 (1995). [3] Mittlefehldt, D.W. (1994) *Meteoritics* **29** 214-221. [4] Valley, J.W., et al. (1997) *Science* **275** 1633-1638. [5] Saxton, J.M., I.C. Lyon, and G. Turner (1998) *Earth and Planetary Science Letters* **160** 811-822. [6] Leshin, L.A., et al. (1998) *Geochimica Et Cosmochimica Acta* **62** 3-13. [7] Eiler, J.M., et al. (2002) *Geochimica Et Cosmochimica Acta* **66** 1285-1303. [8] Romanek, C.S., et al. (1994) *Nature* **372** 655-657. [9] Harvey, R.P. and H.Y. McSween (1996) *Nature* **382** 49-51. [10] Scott, E.R.D., A. Yamaguchi, and A.N. Krot (1997) *Nature* **387** 377-379. [11] McKay, D.S., et al. (1996) *Science* **273** 924-930. [12] McSween, H.Y. and R.P. Harvey (1998) *International Geology Review* **40** 774-783. [13] Warren, P.H. (1998) *Journal of Geophysical Research-Planets* **103** 16759-16773. [14] Hervig, R.L., et al. (1992) *International Journal of Mass Spectrometry and Ion Processes* **120** 45-63. [15] Jull, A.J.T., et al. (1998) *Science* **279** 366-369. [16] Chacko, T., et al. (1991) *Geochimica Et Cosmochimica Acta* **55** 2867-2882. [17] Stiller, M., J.S. Rounick, and S. Shasha (1985) *Nature* **316** 434-435. [18] Sofer, Z. and J.R. Gat (1975) *Earth and Planetary Science Letters* **26** 179-186. [19] Gross, M.G. and J.I. Tracey (1966) *Science* **151** 1082-1083. [20] Amundson, R. and E. Kelly (1987) *Geochimica Et Cosmochimica Acta* **51** 2883-2890. [21] Michaelis, J., E. Usdowski, and G. Menschel (1985) *American Journal of Science* **285** 318-327. [22] Usdowski, E., J. Hoefs, and G. Menschel (1979) *Earth and Planetary Science Letters* **42** 267-276. [23] Clark, I.D., J.C. Fontes, and P. Fritz (1992) *Geochimica Et Cosmochimica Acta* **56** 2041-2050. [24] Anders, E. (1996) *Science* **274** 2119-2121. [25] Carr, M.H.M.H., *Water on Mars / Michael H. Carr*. 1996., New York :: Oxford University Press,.

MGS/TES–Odyssey/THEMIS-IR Analysis of Localized Low Albedo Regions in Valles Marineris. E.Z. Noe Dobrea¹, J.F. Bell III¹, M.J. Wolff², and K.J. Snook³, ¹Center for Radiophysics and Space Research – (406 Space Sciences Building – Cornell University – Ithaca NY – 14853 email: ezn1@cornell.edu), ²Space Science Institute, Augusta GA, ³NASA/Johnson Space Center, Houston TX.

Introduction: We are conducting a systematic analysis of small (~10's of km), localized regions in Valles Marineris that display significant albedo differences relative to their surroundings. This analysis is based on a finding that the locations of the hematite deposits identified by [1] in the interior layered deposits of Valles Marineris typically coincide with regions having a low MGS/TES visible bolometric albedo [1,2]. Until recently, it was difficult to identify the morphology or geologic context of the regions containing the hematite deposits. However, with the recent advent of high-resolution (1/128°/pixel) MOLA gridded topography and Mars Odyssey's THEMIS-IR instrument, it has been possible to better understand the morphologic context of TES observations. This analysis combines the use of PDS-released data from the MGS/TES visible bolometer and infrared spectrometer, the Odyssey/THEMIS Infrared imager, and MOLA gridded topography. First, the TES infrared bolometer is used to identify regions of interesting albedo variability, and is overlaid on Viking controlled photomosaics for context. THEMIS-IR data, in conjunction with MOLA topography, is then used to: 1) identify the context and morphology of the area; and 2) identify spectrally unique regions at the km scale. In preparation for the latter, all the THEMIS planes are coregistered using an autocorrelation routine, the data are converted to brightness temperature and then each plane is normalized to the brightness temperature of the third plane (1261 cm⁻¹). We then perform a 3-band search for color variations and a Principle Components Analysis (PCA) of the 8 unique bands in the THEMIS-IR dataset. Any variability is then investigated using both THEMIS-IR and TES spectra of the same regions. In both cases, the spectra are ratioed to near-simultaneously acquired spectra of adjacent or "average" regions that do not show this albedo variation, therefore allowing us to identify spectral variability unique to the area of interest. This procedure also allows us to account for calibration problems in THEMIS-IR data, and for any atmospheric effects in both the THEMIS-IR and the TES data.

Observations: One example presented here is a low albedo region in central Ophir Chasma (3.6°S, 73.0°W) that has not been identified as a hematite rich-deposit. This region is located at the base of the interior deposits and north of the largest hematite deposit found in Ophir Chasma [1]. It has a relatively low TES albedo (0.17) compared to that of the sur-

rounding region (0.20) and of the brighter highland plains (0.25) (see Figure 1). THEMIS-IR images and MOLA gridded topography show that this area contains a 100 km² region in a topographic low at the base of the layered floor deposits (see Figure 2). Its brightness temperature at 1261 cm⁻¹ is approximately 10K greater than that of the average non-shadowed surrounding terrain.

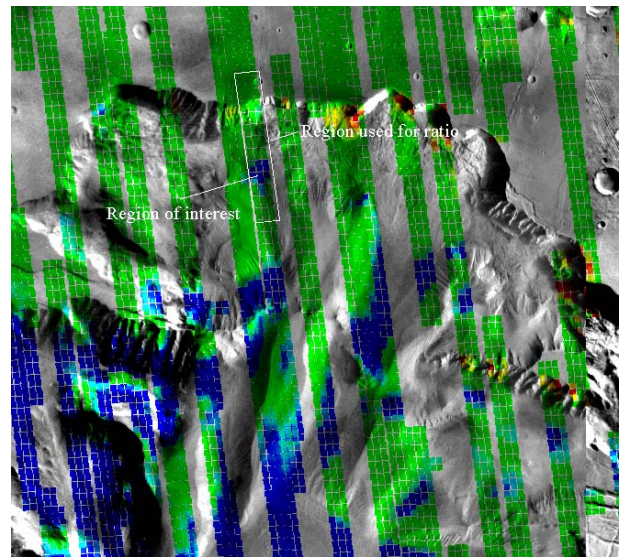


Figure 1: TES visible bolometer data overlaid on a Viking control photomosaic of Ophir Chasma. Note the lower albedo of the region of interest relative to the surrounding terrain. The next low albedo region south of this area along the same strip corresponds to the deposit with the greatest concentration of gray hematite found in Ophir Chasma by [1].

The THEMIS-IR spectrum of this region (cyan) mirrors the spectrum of the highland plains immediately north of Valles Marineris (maroon) and the relative brightness temperature of this region is well below the average spectrum of the entire region (red—line of ratioed value of 1) for all wavelengths except 795 cm⁻¹ (see Figure 3). The spectral differences between the low albedo region and plains region are consistent with the effects of suspended atmospheric dust: because the plains are higher elevation than the average scene (which includes both the plains and the chasma), we see an inverted dust absorption relative to the average. The opposite is true for our low albedo region of interest. The spectra of the regions shown in blue and light green in Figure 2 behave similar to the cyan region, and are therefore not plotted. However, it is worth

noting that the spectra of the interior layered deposits show significant spectral variability not consistent with atmospheric absorption. Of particular interest is the spectrum of a layer in the deposits themselves (dark green), which shows absorptions relative to the average spectrum at both 979 and 848 cm^{-1} . Unfortunately, this feature is too small to be detected by TES. However, the terrain responsible for the variability in the yellow and magenta spectra is large enough (km in size) that it should be detectable using TES.

TES spectra of the region (Figure 4, top), ratioed to the average spectra of immediately adjacent higher albedo regions does not appear to show the differences observed in the THEMIS-IR data. On the other hand, this ratio spectrum does show a positive slope in the low wavenumber region ($200\text{--}600\text{ cm}^{-1}$) and a broad, shallow band between 800 and 1200 cm^{-1} . Neither of these two features are present in identically-ratioed adjacent spectra. Even if the broad band corresponds to different optical depths through the atmospheric dust, the slope cannot be accounted for by atmospheric effects based on our modeling of dust absorption in the atmosphere.

Interpretation: Due to the fact that the largest absorptions found in the layered terrain correspond to only 0.06% variability in THEMIS-IR data relative to an average spectrum of the region, care must be taken when considering the validity of the observation. However, if the two absorptions found in the layers of the interior deposits of Valles Marineris are real, they require there to be either one material with those two absorption features, or more than one different materials whose spectra mix linearly to generate such features. Comparison of the THEMIS-IR spectra of the layers with data from the ASU's mineral spectral library [3] yields only two minerals that exhibit both observed features. These minerals, bronzite and enstatite, are both orthopyroxenes typically found in volcanic rocks. If we assume instead that each feature is generated by one mineral, we find that practically all the minerals that possess either one of those two bands are silicates (including plagioclases, pyroxenes, amphiboles, and serpentines). All of these can be found in volcanic rocks, although the latter two hydroxides can also be formed as volcanic alteration products.

Interpretation of TES spectra is more complicated because the only minerals in the ASU spectral library that contain a positive, featureless slope at small wavenumbers tend to be fine-grained clays. However, this is not necessarily indicative of clays, as the spectra for many fine-grained materials like these have not been published in this spectral regime.



Figure 2: THEMIS-IR 3-band ratio view of the low-albedo region found in TES data (region encompassing green dot). Each band was ratioed to band 3. Note other similar regions in the image (cyan dot), and the well-defined layers at the bottom of the image.

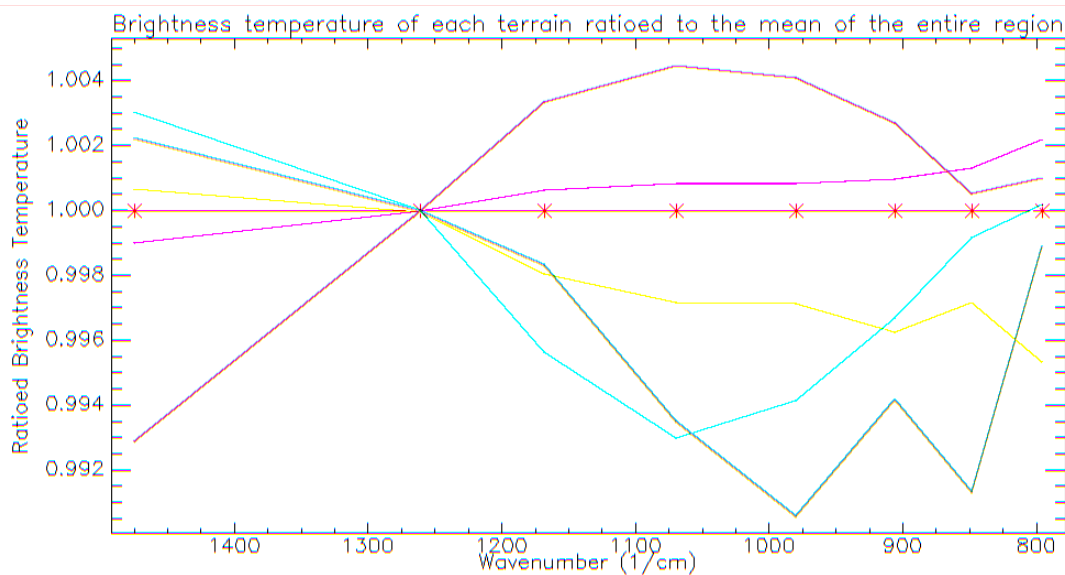


Figure 3: THEMIS-IR spectra of the regions highlighted in Figure 2. Each spectrum has been divided by an average spectrum of the entire region shown in Figure 2 (red) and extending northward into the plains north of the Chasma (not shown). Note the mirroring effect of the spectra of our region of interest (cyan) to that of the highland plains (maroon) about the axis of the (red) average terrain line. This effect is caused by atmospheric dust absorption. Also note the relatively strong absorption band of the layers (dark green).

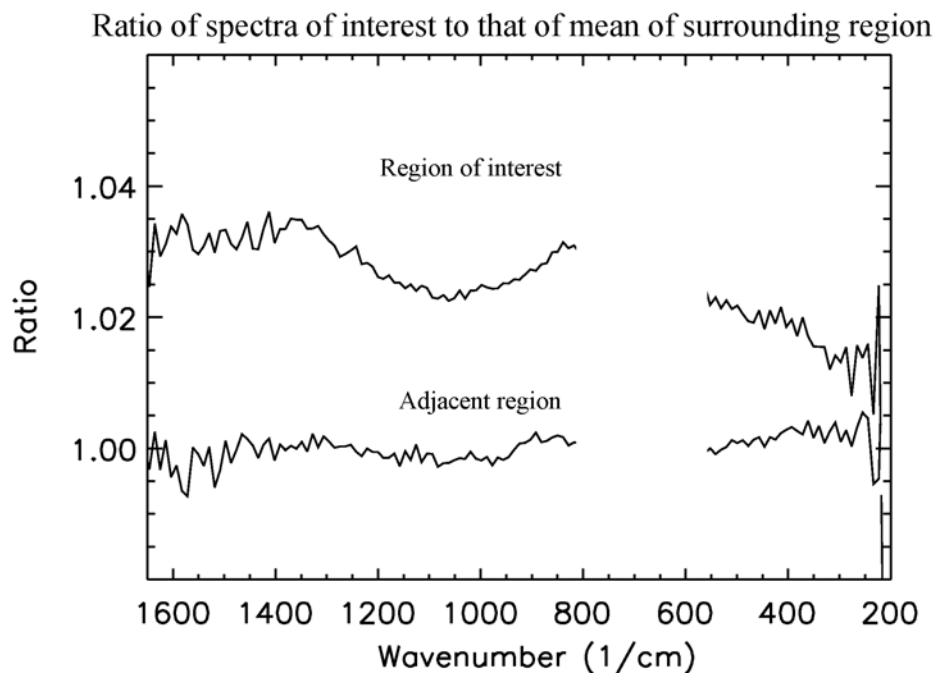


Figure 4: TES spectra of our low albedo region of interest ratioid to an average spectrum of the region defined in Figure 1. Note the positive slope in the spectrum at low wavenumbers and the broad absorption feature between 800 and 1200 cm^{-1} . Note that the similarly-ratioid spectrum of an immediately adjacent, higher albedo region does not show these features.

References: [1] Christensen, P.R. *et al.* (2001) *JGR*, 106, 23,873-23,885. [2] Noe Dobrea, E.Z. *et al.* (2002) AAS DPS abstract #34, #03.05. [3] Christensen, P.R. *et al.* (2000) *JGR*, 105, 9735-9738.

SEASONAL/DIURNAL MAPPING OF OZONE AND WATER IN THE MARTIAN ATMOSPHERE.

R. E. Novak¹, M. J. Mumma², M. A. DiSanti², N. Dello Russo³, K. Magee-Sauer⁴, B. Bonev⁵, ¹Iona College, New Rochelle, NY 10801-1830, rnovak@iona.edu, ²NASA/GSFC, Greenbelt, MD 20771-0003, ³Catholic University of American, Washington DC 20064-0001 and NASA/GSFC, Greenbelt, MD 20771-0003, ⁴Rowan University, Glassboro, NJ 08028-1702, ⁵Ritter Astrophys. Res. Ctr., University of Toledo, Toledo OH 43606

Introduction: Ozone and water are key species for understanding the stability and evolution of Mars' atmosphere; they are closely linked (along with CO, H, OH, and O) through photochemistry [1-4]. Photolysis of water produces the OH radical (thought to catalyze reformation of CO₂ from CO and O₂) and atomic hydrogen (which reacts with O₃ forming OH and O₂). Atomic hydrogen also reacts with O₂ (forming HO₂), thereby reducing the amount of O₂ available to reform O₃ from collisions between O and O₂. Hence ozone and water should be anti-correlated on Mars.

Photolysis of O₃ produces O₂(a¹Δ_g) with 90% efficiency [5], and the resulting emission band system near 1.27 μm traces the presence and abundance of ozone. This approach was initially used to study ozone on Earth [6] and then applied to Mars [7]. In 1997, we measured several lines of the O₂(a¹Δ_g) emission (Fig. 1.) using CSHELL [8] at the NASA IRTF; the O₂(a¹Δ_g) state is also quenched by collisions with CO₂. This quenching dominates at lower altitudes so that the detected emissions are used to detect ozone column densities above ~20 km. The slit was positioned N-S along Mars' central meridian resulting in a one-dimensional map of ozone [9].

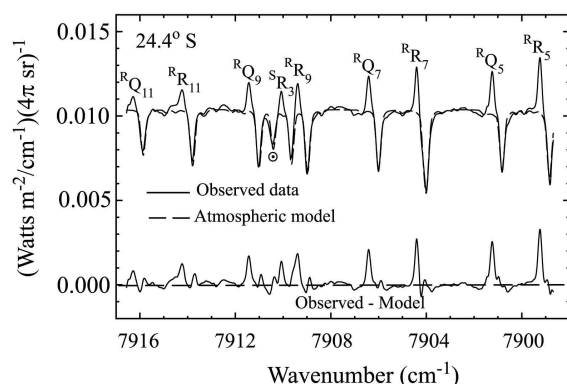


Fig. 1. Spectral extract (summed over one arc-second) on Mars centered at 24.4° S latitude, 2:20 PM local time on Jan 21, 1997 ($L_s = 67^\circ$). The continuum is sunlight reflected from Mars' surface. Emission lines from the O₂(a¹Δ_g) state are labeled. The synthetic terrestrial atmospheric model is indicated by the dashed trace. The difference between the observed spectrum and the atmospheric model reveals the isolated O₂(a¹Δ_g → X³Σ_g) emission from Mars' atmosphere (lower trace). A Boltzmann analysis of the emis-

sion lines determines a rotational temperature (175 ± 5 K), and the column density above ~20 km (2.8 ± 0.2 μm-atm) [9].

Nearly simultaneous maps may be made of water using CSHELL by detecting the *n*₁ fundamental band of HDO near 3.67 μm (Fig. 2) and using the D/H ratio for Mars [10]. This technique was used by DiSanti and Mumma [11]. With CSHELL, measurements for both O₂(a¹Δ_g) emissions and HDO absorptions can be made during the day or night.

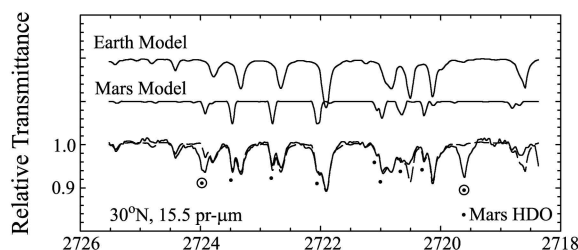


Fig. 2. Detection of HDO on Mars Jan 21, 1997 ($L_s = 67.3^\circ$). The observed spectral trace (solid curve-bottom plot) is an extract summed over 1.0 arc-sec on Mars. The upper traces are atmospheric transmittance models generated for the Earth and Mars (Doppler-shifted); these are combined and plotted as the dashed trace with the observed spectrum. The best fit between the HDO lines of the observed spectrum (indicated by dots) and the convolved model provides the column abundance of water on Mars. A D/H ratio of 5.2 times the standard mean ocean water ratio was adopted [10]. Solar Fraunhofer lines are also detected [9].

Since January, 1997, we have repeated these measurements at different times during the Martian year (Table I). For all of these dates, we have positioned the slit N-S along the central meridian; for some of these dates, we have also stepped the slit across the planet at 1 arc-sec intervals generating a 2-dimensional map. We have also positioned the slit E-W on Mars thus providing diurnal variations of ozone and water along the slit.

Seasonal Variation of Ozone and Water: A summary of our observations taken at four different times during the Martian year appears in Fig. 3. The largest measured column density of ozone appears near

aphelion ($L_s = 67^\circ$). The measured ozone (column density above 20 km) is large in both hemispheres, but is not seen to be anti-correlated with the measured water density. Furthermore, a decrease in the measured ozone level appears near the sub-solar (23.5° N) location. Our measurements of ozone were taken close in time to those taken with the Faint Object Spectrometer (FOS) on the Hubble Space Telescope [12]; this instrument measures the total column density of ozone. The CSHELL measurements [9] are consistently smaller than the FOS measurements. The CSHELL measurements also vary smoothly from south to north whereas the FOS measurements show a wider variation in values; the CSHELL measurements have a field of view of ~ 1 arc-sec causing localized variations to average out while the FOS measurements have better spatial resolution on Mars. We believe that both measurements are consistent as explained by an atmospheric model for near-aphelion conditions [13]. Near-aphelion, water vapor is located at altitudes < 10 km; at altitudes above 20 km, water vapor is small and would not affect the ozone density. Since we measure ozone above 20 km, we interpret our ozone measurements to be insensitive to the water measurements located at lower altitudes.

For the $L_s=67^\circ$ measurements, the decrease in ozone density near the sub-solar point has not been sufficiently explained; during this season, ice clouds at mid-latitudes could affect the density of ozone. Another explanation is that the ice clouds prevent some of the ozone from being photolyzed causing a smaller emission from the $O_2(a^1\Delta_g)$ state [14]. This phenomenon requires further analysis.

The measurements at $L_s=103^\circ$ and $L_s=133^\circ$ show a decrease of ozone in the northern hemisphere with the ozone being concentrated in the southern hemisphere during the late northern summer; at this time, the water column density in the north reaches its yearly maximum [15]; also, the water vapor probably extends to higher altitudes causing the ozone level to decrease. This seasonal decrease is not as drastic in the southern hemisphere since the overall water column density there is still relatively low.

Observations taken during early northern winter ($L_s=306^\circ$) show no detectable emissions from the $O_2(a^1\Delta_g)$ state across most of the planet indicating a reduced value of ozone above 20 km. This may be explained using a model for near perihelion conditions [13]. At this season, water vapor extends to higher altitude than at aphelion causing a reduction of ozone above 20 km. Though the water column density in the northern hemisphere is smaller at this time than at

$L_s=67^\circ$, its location at a higher altitude reduces ozone above 20 km.

TABLE I
CSHELL Observations of Mars

UT date	L_s	Del-Dot (km sec ⁻¹)	Diameter
21 Jan 1997	67°	-15.3	9.6"
01 Mar 1997	84°	-7.2	13.4"
20 Mar 1999	112°	-12.7	12.6"
05 Jul 1999	165°	10.5	11.1"
15 Jan 2001	103°	-17.0	5.7"
20 Mar 2001	133°	-16.5	9.2"
10 Jan 2002	306°	13.0	6.0"
13 Jan 2003	124°	-14.9	4.8"
21 Mar 2003	154°	-15.6	6.9"

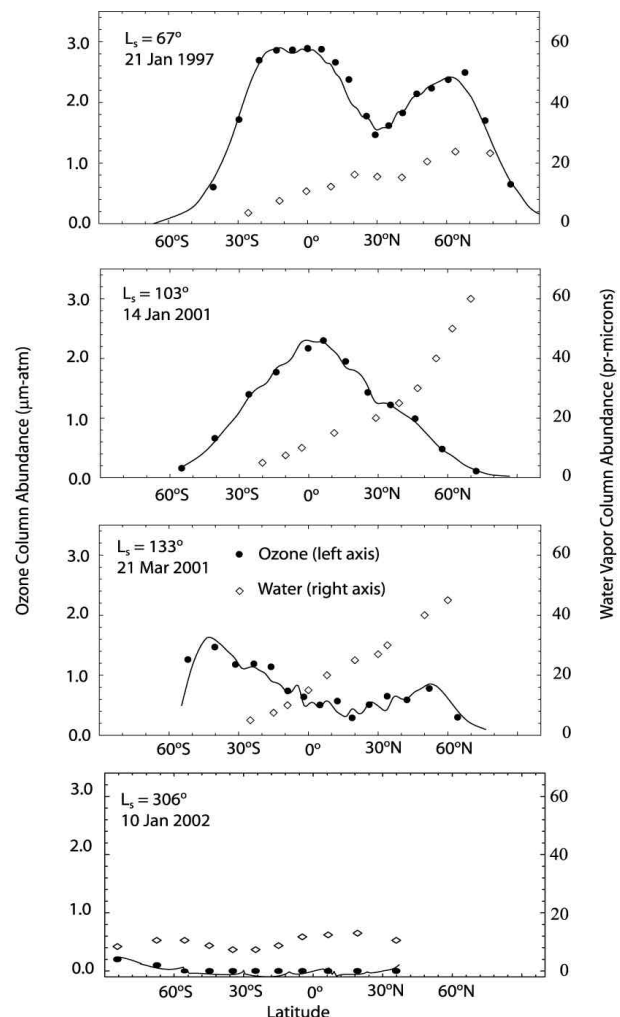


Fig. 3. Water and ozone maps taken at different times during Mars' year using CSHELL. The water measurements are taken by measuring HDO spectra on Mars and using a D/H ratio of 5.2 to obtain water column densities [10]. The data indicate that the relationship between water and ozone also depends on altitude.

A better explanation for the relationship between water and ozone in the Martian atmosphere requires vertical profiles of both molecules; to date, detailed measured profiles are lacking. Our CSHELL measurements provide limited but useful vertical profile information when combined with measurements of the total column density of ozone from space [12] or ground based [16] observations. We plan to determine an "average" altitude for water by performing a Boltzmann analysis on Mars HDO absorption lines (Fig. 4). The retrieved rotational temperature can be compared to altitude profiles of temperature obtained from MGS-TES measurements [15].

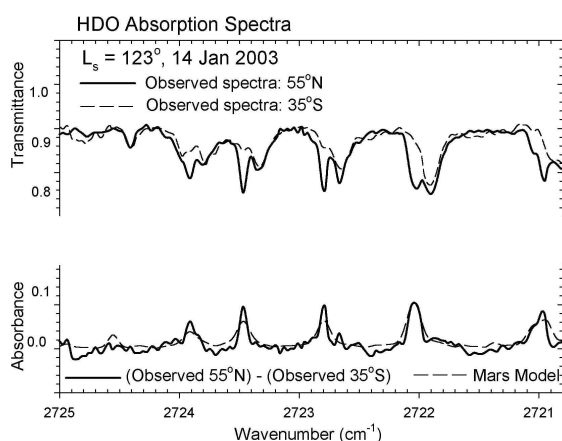


Fig. 4. HDO absorption spectra. Top traces show observations at different latitudes; bottom trace shows difference between the two, canceling the earth's atmosphere and yielding the difference in water column density between the two latitudes.

Diurnal Variation of Ozone: In addition to seasonal effects, ozone is expected to show strong diurnal variation; CSHELL measurements confirm this (Fig. 5). These data were taken with the slit oriented parallel to the equator of Mars and centered at 57°S; the sub-earth point corresponds to 2:00 PM local time. The presented Mars emissions are taken at equal air-masses (1.6 arc-sec either side (11:00 AM and 5:00 PM) of the sub-earth point); the decrease in emission intensity indicates a decrease in ozone towards late afternoon; the observed terminator was in the evening sky. Ozone is regenerated during the night ($O + O_2 + M \rightarrow O_3 + M$; $OH + O_2 \rightarrow H + O_3$), and a measure near dawn will permit an assessment of this production. Observing the morning terminator, which is available after apparition, will enable us to measure the regenerated ozone and to follow its photolysis through late afternoon.

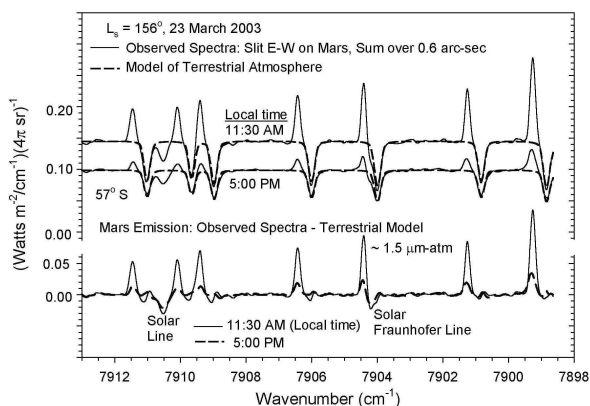


Fig. 5. Observed spectra (O_2 $^1\Delta$) emissions) taken with the slit E-W on Mars and centered at 57°S. The two observed spectra are 1.6 arc-sec either side of the sub-earth points (11:00 AM, 5:00 PM local time). A terrestrial model is subtracted from the observed spectra yielding O_2 ($^1\Delta_g$) emission lines in the Mars spectra that are Doppler shifted from the corresponding earth absorptions. Decrease in the O_2 ($^1\Delta_g$) emission through the day results from photo-destruction of ozone by the UV Hartley band.

Future Plans: Our goal is to take observations throughout the entire Martian year. Mars' eccentric orbit leads to ~45% more insolation at perihelion than aphelion; this results in the large difference between northern summer and southern summer as shown by data taken at $L_s = 103^\circ$ and $L_s = 306^\circ$ in Fig. 3. Our observations require Doppler shifts greater than 10 km sec^{-1} in order to distinguish Mars' spectra from the earth's. Seasonal gaps in our database exist between $L_s = 165^\circ$ and $L_s = 306^\circ$ and between $L_s = 306^\circ$ and $L_s = 67^\circ$; during the time period of the latter gap, the ozone column density is expected to increase drastically across the planet. January – April, 2004 will provide the opportunity to observe Mars between $L_s = 330^\circ$ and $L_s = 10^\circ$. Continued mapping with the slit E-W will provide information on both the photo-destruction and the regeneration of ozone above 20 km.

Acknowledgments: This work was supported in part by grants from NASA (RTOP 693-344-32-31) and the NSF (AST-0205397). Data presented herein were obtained at the NASA Infrared Telescope Facility (IRTF), which is operated for NASA by the University of Hawaii. We gratefully acknowledge the support of the IRTF Director and the expert assistance of the IRTF telescope operators and staff.

References: [1] Hunten, D. M. (1974) *Rev. Geophys. Space Phys.* 12, 529-535. [2] Krasnopolsky, V.A. (1993) *Icarus* 101, 313-332. [3] Nair, H., et al. (1994) *Icarus* 111, 124-150. [4] Yung, Y.L. and W. B. DeMore (1999) *Photochemistry of Planetary Atmos-*

pheres, Oxford University Press, New York. [5] Ball, S.M. et al. (1993) *Geophys. Res. Let.* 20, 2063-2066. [6] Noxon, J.F. (1968). *Sp. Sci. Rev.* 8,92-134. [7] Noxon et al. (1976) *Ap. J.* 207,1025-1035. [8] Tokunaga, A. T et al.*Proc. SPIE* 1235, 131-143. [9] Novak, R. E. et al. (2002), *Icarus* 158, 14-23. [10] Bjoraker, G. L. et al. (1989) *B.A.A.S.* 21, 991. [11] DiSanti, M.A. and M.J. Mumma (1995) *Workshop on Mars Telescope Observations* (Cornell U. Press). [12] Clancy, R. T., et al. (1999) *Icarus* 138, 49-63. [13] Clancy, R.T. and H. Nair (1996) *J. Geophys. Res.* 101(E5), 12785-12790. [14] Pearl, J.C. et al. (2001) *J. Geophys. Res.* 106, 12325-12338. [15] Smith, M.D. (2001) *J. Geophys. Res.* 106, 23929-12945. [16] Espenak, F. et al. (1991), *Icarus* 92, 242-262.

EVIDENCE FOR A SURGING ICE-SHEET IN ELYSIUM PLANITIA, MARS. J. Nussbaumer¹, R. Jaumann², and E. Hauber², ¹GeoForschungsZentrum Potsdam, Div. 1 Geodesy and Remote Sensing, D-14473 Potsdam, Germany; jnussbau@gfz-potsdam.de. ²DLR Institute for Space Sensor Technology and Planetary Exploration, Rutherfordstr. 2, D-12489 Berlin, Germany; juergen.nussbaumer@dlr.de.

Introduction: High resolution Viking images (orbit 724A, 14m/pixel) show evidence for ancient glaciation in parts of southeastern Elysium Planitia. While previous authors have mapped the materials as thin lacustrine and fluvial deposits [1], we present evidence for erosional and depositional processes associated with glacial environments. The previous ice sheet formed hummocky groundmoraines, eskers, and possibly pingos.

Geomorphology: Detailed geomorphological

mapping of high resolution Viking Orbiter images reveals several features which can be attributed to glacial and periglacial processes in the southeastern part of Elysium Planitia (Fig. 1).

Ground moraines. The presence of a former ice sheet is indicated by hummocky terrain resembling terrestrial ground moraines. A sharp contact marks the boundary between the ice sheet and an adjacent yardang field.

Eskers. The ground moraine is locally overlain by

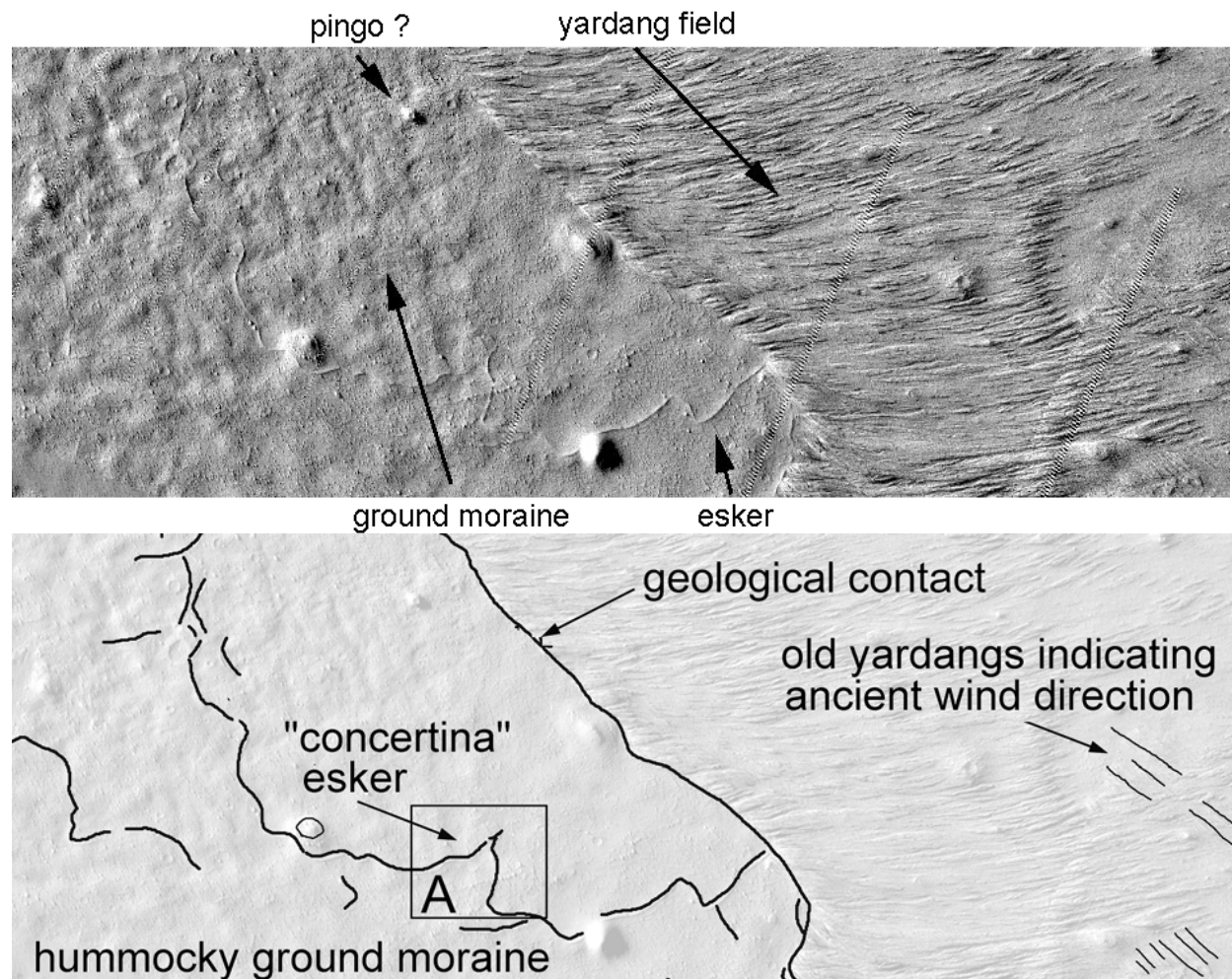


Figure 1: Image mosaic of Viking orbit 724A (14m/pixel; image width 60km, North is up, center at 207°W, -3°S) and geomorphological sketch map. Hummocky groundmoraines, eskers, and possibly pingos are evidence for former glaciation. The outlined box A marks the location of eskers deformed into a zigzag pattern typical for terrestrial *concertina eskers* (compare with box A' in Fig. 2).

mostly curvilinear features. They are interpreted as eskers, sinuous ridges of glacial sand or gravel formed as infillings of ice-walled rivers [2,3]. Locally, the sinuous pattern of the eskers (as seen in plan view) is changed into a jagged or zig-zag path. On Iceland, previously sinuous eskers have been shortened and crumpled into such a zigzag pattern by the advancing glacier snout (Fig. 2) [4,5]. These so-called *concertina eskers* are associated with *surging glaciers*, characterized by periodic changes in flow velocities over various timescales [6]. It is important to note that the surges are NOT triggered by climatic oscillations, but by oscillations in the internal workings of the glacier [7]. Therefore, although it is tempting to ascribe the former existence of a possible surging glacier on Mars to previous climatic changes, this assumption is not supported by terrestrial analogy.

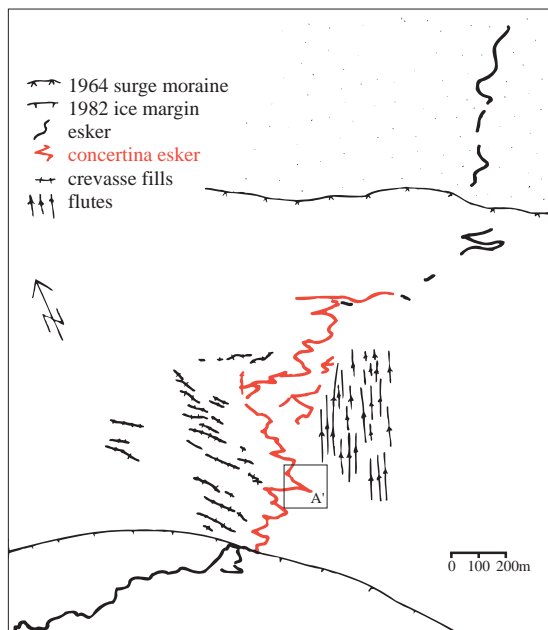


Figure 2: Sketch map of concertina eskers associated with the Bruarjökull glacier in Iceland. Eskers are deformed by the advance of the glacier snout. Note the similarity of the feature in the outlined box A' with the esker in box A of Fig. 1 (modified from [5]).

Pingos. Several circular hills are distributed on the ground moraine, partly characterized by depressions on their top. They are interpreted as pingos, ice-cored hills formed in periglacial environments on Earth by the intrusion and subsequent freezing of pressurized water or by the growth of ice lenses [2,3].

Boulder trains. Boulder trains are widespread on the ground moraine (Fig. 3). While they also occur in the lee of obstacles in large floods or downslope from outcrops on steep slopes, they can also be associated

with glacial deposits [8]. There, they indicate the direction of ice movement during the last stage of glaciation [9].

Conclusions: Several landforms in southeastern Elysium Planitia suggest previous local or regional glaciation. The relatively young age (Amazonian, see [1]) and the geographic location near the equator bears important paleoclimatic implications. Further investigations (especially more detailed age determinations by crater counting and high resolution imagery by the *Mars Observer Camera* or future instruments) are required to confirm or reject the possibility of near equatorial glaciation in the comparably recent past of Mars.

References: [1] Scott, D.H. and Chapman, M.G. (1995) USGS Map I-2397. [2] Washburn, A.L. (1973) *Periglacial Processes and Environments*, Edward Arnold, London. [3] French, H.M. (1976) *The Periglacial Environment*, Longman, London. [4] Sharp, M. J. (1985) *Quaternary Research*, 24, 268-284. [5] Knudsen, O. (1995) *Quaternary Science Reviews*, 14, 487-493. [6] Benn, D.I. and Evans, D.J.A. (1998) *Glaciers and Glaciation*, John Wiley, New York. [7] Meier, M. F. and Post, A. S. (1969) *Canadian Journal of Earth Sciences*, 6, 807-819. [8] Lucchitta, B.K. (1998) *LPS XXIX*, 1287-1288. [9] Sugden, D.E., Glasser, N.F., and Clapperton, C.M. (1992) *Geografiska Annaler*, 74A, 253-264.

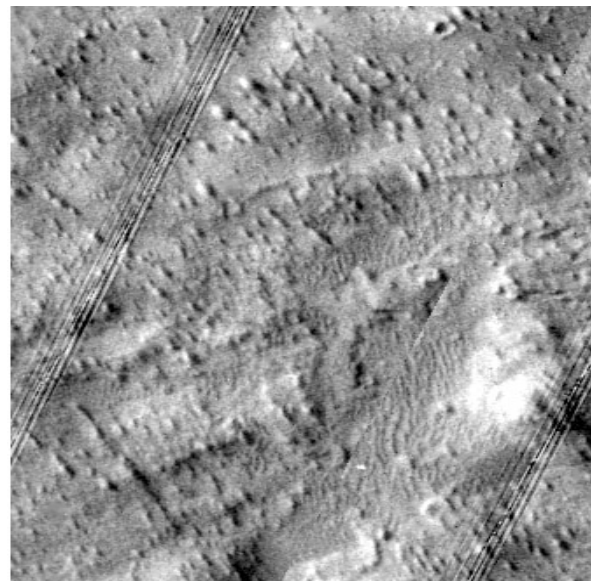


Figure 3: Boulder trains possibly related to a pulse of erosion at the end of the last glacial cycle when the ice was thin [9]. They also indicate ice movement from SE towards NW (topographic data from the *Mars Observer Laser Altimeter* show that topographic gradient is towards NW; Viking orbit 724A, width of image 10 km, North is up).

MELTING OF THE MARTIAN PERMAFROST BY HYDROTHERMAL CONVECTION ASSOCIATED WITH MAGMATIC INTRUSION. Y. Ogawa¹, Y. Yamagishi² and K. Kurita¹, ¹Earthquake Research Institute, University of Tokyo 1-1-1, Yayoi, Bunkyo-ku, Tokyo, (Yoshiko@eri.u-tokyo.ac.jp), ²Institute for Frontier Research on Earth Evolution, Japan Marine Science and Technology Center, Yokosuka.

Introduction: Many surface features on Mars are closely connected with the subsurface permafrost layer. The polygonal fractures and the possible thermokarsts are observed on the martian surface and they are analogous to the terrestrial features located on the permafrost. The rampart and/or fluidized ejecta morphology of martian craters is indicative of subsurface volatiles. Mars should stock much water in a form of ground ice.

The suspected fluvial features on Mars would suggest water (or its mixture), which is coming from the subsurface aquifer or the ground ice. Such a martian hydrothermal system has been the alternative idea to the assumption of precipitation for forming observed fluvial-like features on Mars. The outflow channels, in particular, have characteristics unique to water erosion and clearly indicates the surface runoff of huge amount of water [1], [2], which usual precipitations could not supply. The outflow channels potentially suggest the pre-existence of a substantial amount of liquid water very close to the martian surface to cause a large flood. The idea of supplying such massive liquid water near the ground might be still controversial, however, from many observational facts, we assume that the igneous melting of the martian permafrost layer should have played a significant role. We have numerically simulated the generation of meltwater and are proposing a consistent scenario of forming the outflow channels as well as the headwater regions; chaotic terrains [3].

Igneous Melting of the Subsurface Permafrost Layer: We numerically simulate the melting process of the permafrost layer induced by magmatic intrusion [3]. The shape of the intrusive body has a significant effect on the development of the melt region. The permafrost is modeled as a porous medium in which the matrix is rock and the pores are filled with water ice. Several types of porosity distribution are assumed. The point of our simulation is incorporation of thermal convection in porous media, which has not been modeled well in previous studies of the melting of the permafrost.

Our main results show that convection in the melted zone causes drastic change in heat transfer, which results in focussing the growth of the melt region and enhancement of water generation. The resulting melt zone extends vertically up just next to the surface, like a plume with a single column (mushroom structure) as seen in Figure 1. τ is the dimensionless time (normal-

ized by H^2/κ , κ : thermal diffusivity of water) and the zone which is about a size larger than the yellow region corresponds to the melted zone. Lastly, we see, that the hot zone spreads laterally ($\tau > 0.17$) in equilibrium state.

The behavior of the system is mainly controlled by the two non-dimensional parameters; the Rayleigh (Ra) number and the Stefan number (Ste). The Ra represents the strength of the thermally-driven natural convection in a porous medium and the Ste represents the measure of thermal contribution of the phase change [3]. The development of the meltwater volume with the time is shown in Figure 2. The pure conduction case is illustrated as a reference, showing only a gradual rise in water volume with time. This contrasts with an abrupt rise in meltwater production associated with the initial and middle stages of convection. Here the volume shown is normalized by $3H^2D$ (H: thickness of the permafrost layer, D: the depth) and time is non-dimensional.

Martian Hydrothermal Systems: The melting process within the permafrost driven by the thermal convection, which we revealed in the previous section, produces a substantial amount of water very close to the surface. In response to compaction in this region, segregated liquid water is expected to form a subsurface pool and may have erupted out of the ground to form the fluvial features. Liquefaction might happen, too, which could result in the similar catastrophic process. Such events would certainly be accompanied by surface destruction, which we can see as chaotic terrain.

We are proposing a consistent scenario of forming surface features around the outflow channels (Figure 3).

The implication of the melting of the permafrost is not restricted to the formation of chaotic terrains. Other features settled in headwater regions of channels could possibly be influenced by this melting process of the subsurface permafrost layer.

We direct our attention to each of such surface features. We will report on results of simulation with more plausible parameters, especially considering the morphology of the magmatic intrusion. Recently Scott et al. [4] and Wilson and Head [5] showed the probable population of giant dikes from the Tharsis area. The sill intrusion was also discussed on the Ascraeus Mons based on the geologic analysis [6]. Considering the newly revealed observational facts, we simulate the

melting process for the more realistic case targeting at each of the observed features.

In the modeling, we also modify our previous simple assumptions, introducing the vertical distribution of the porosity of the permafrost layer and evaluating the thermal history of the magmatic body intruded.

Summary: We have quantitatively assessed the effect of thermal convection on enhancing and focusing heat transfer in melting of the permafrost on Mars. The resulting melt zone extends up to just beneath the surface, creating a plume with a mushroom structure. The resulting volume of meltwater is several times as much as that expected in the conduction case. These two characteristics mean that substantial amount of meltwater could exist very near to the surface, which should effect on the possible hydrothermal systems on Mars considerably. We applied our numerical simulation to the plausible area on Mars where the interaction of magma and permafrost is expected, modifying our model and introducing the more realistic parameters based on the latest observation.

References:

[1] Baker, V. R. and Milton, D. J. (1974) *Icarus*, 23, 27-41. [2] Baker, V. R. (1982) *The channels of Mars*, Univ. of Texas Press. [3] Ogawa, Y. et al. (2003) *JGR*, 2002JE001886 (in printing). [4] Scott, E. D. et al., (2002) *JGR*, 107, (E3), 10.1029/2000JE001431. [5] Wilson, L. and Head, J. W. (2002) *JGR*, 107, (E8), 10.1029/2001JE001593. [6] Scott, E. D. and Wilson, L. (1999) *JGR*, 104, 27,079-27,089.

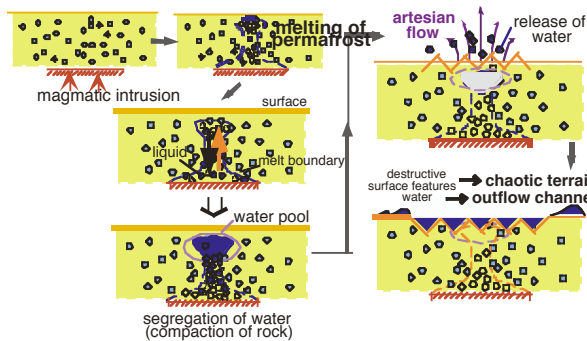


Figure 3. A scenario for the origin of chaotic terrain and outflow channels, quoted from Ogawa et al., 2003.

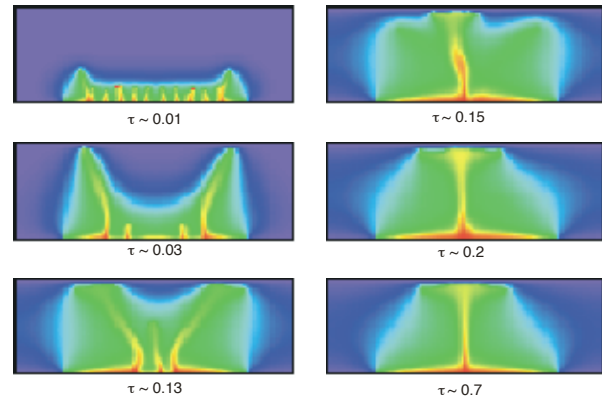


Figure 1. Evolution of temperature field within the martian permafrost layer with igneous heating, quoted from Ogawa et al., 2003. τ is dimensionless time and the zone which is about a size larger than the yellow region corresponds to the melted zone. The zone extends vertically with time and extends almost to the surface. Lastly, the hot zone spreads laterally ($\tau > 0.7$) in equilibrium state.

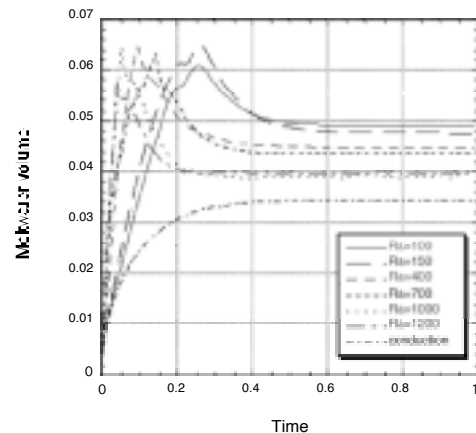


Figure 2. Production of meltwater as a function of time for various Ra: 100-1200, quoted from Ogawa et al., 2003. The pure conduction case is illustrated as a reference, showing only a gradual rise in water volume with time. This contrasts with an abrupt rise in meltwater production associated with the initial and middle stages of convection. Volume is normalized by $3H_2D$ (H : thickness of the permafrost layer, D : the depth). Time is non-dimensionalized by H^2/α (α : thermal diffusivity of water).

SUBSURFACE EXPLORATION FOR WATER ON MARS

G. R. Olhoeft (Colorado School of Mines, 1500 Illinois St., Golden, CO 80401-1887 USA golhoeft@mines.edu).

Introduction: Water is involved in many geological and biological processes and has many unusual properties. The unique detection of water requires looking for a method that can characterize something unique about the existence or occurrence of water or of some process that is a result of the behavior of water. There are many methods that can detect the presence of water but few that can unambiguously and uniquely identify it as being water. Most methods rely on detecting the motion of all or parts of the water molecule [1]. Each method has advantages and disadvantages in subsurface exploration, but those that are the most unambiguous detectors of water do not work to adequate depths of exploration (hundreds of meters to kilometers). The methods that can least ambiguously detect water to depths of kilometers are combined electromagnetic and seismic exploration for the Bjerrum defect dielectric and elastic relaxation process in water ice and the seismoelectric coupled process for liquid water in a pore space.

Electromagnetic Exploration: By exciting motion in charged particles, electromagnetic waves are generated. The interaction of these waves with matter is a function of the frequency of excitation of the wave. At low frequencies (below 1 MHz), these waves diffuse into the ground through a process called electromagnetic induction, and there are many methods and techniques available to use EM induction for subsurface exploration [2]. At high frequencies (above 1 MHz), the waves propagate and the most common exploration method is called ground penetrating radar [3]. The depth of subsurface exploration is a function of material properties and frequency, with lower frequencies penetrating deeper. The resolving ability of the methods general improves with increasing frequency. Grimm [4] and Olhoeft [5] have reviewed the prospects for low and high frequency electromagnetic systems on Mars.

These electromagnetic systems respond to geometry and the material properties characterized by electrical conductivity, dielectric permittivity, and magnetic permeability [6]. The electrical conductivity and dielectric permittivity of soils and rocks are a function of their water content and properties. Water presence has no impact on magnetic permeability (unless water changes iron oxidation state by corrosion). At low frequencies, the electrical conductivity is a very sensitive indicator of the amount, chemistry, state and distribution of water [7]. However, there are a large number of factors that determine electrical

conductivity, making it a very nonunique detector of water.

Frozen water as ice Ih has a Bjerrum defect in its structure which results in a dielectric relaxation process in the kilohertz frequency range [8]. The detection of the frequency response of this dielectric relaxation is a less ambiguous indicator of water. It is not unique, however, as geometry or magnetic relaxation processes [9] may also possibly produce similar responses in electromagnetic exploration systems.

Seismic Exploration: If instead of propagating an electromagnetic wave, a physical particle motion is excited, then an elastic wave will propagate and seismic methods of subsurface exploration are employed. As in electromagnetic methods, lower frequencies penetrate deeper but higher frequencies have higher resolution. The same defect in ice as produced the dielectric relaxation in the kilohertz frequencies also produces an elastic relaxation response [8]. Finding both the dielectric relaxation with an electromagnetic measurement and the elastic relaxation with a seismic or acoustic measurement produces not only a unique indicator of water ice, but it also indicates the temperature of the ice.

The viscous motion of liquid water inside a pore space is one of the main causes of attenuation for elastic wave propagation [10, 11]. The lack of water on the moon is the reason why the low frequency seismic attenuation is so low [12]. High frequency attenuation is dominantly by scattering.

Water Exploration: The search for subsurface water at depths greater than one meter is relatively difficult. To first order, the seismic Q is a good large volume average indicator of water presence. If the Q is in the thousands or higher like the Earth's moon, then there is no significant water present. If the Q is in the tens, then water is present in the subsurface comparable to the Earth. In between, the details of the Q versus frequency from a few hertz to kilohertz will indicate the amount and form of water (liquid or frozen). Around a few hertz, both seismic and electromagnetic measurements can penetrate to kilometers depth of investigation.

If the seismic Q versus frequency and the electromagnetic Q versus frequency show relaxation processes in the kilohertz region, then the Bjerrum defect model [8] can be used to identify and estimate the amount of frozen water ice Ih present and the temperature of the ice. Kilohertz depth of penetration may be as much as kilometers for electromagnetic

methods, but will likely be hundreds of meters or even much less for seismic methods. This requires confirmation that there are no obscuring or confusing magnetic relaxation processes present, and it requires information about electromagnetic and seismic noise levels.

If the electrical conductivity is very low at low frequencies, then little liquid water is present. If it is very high, then the possibility exists for significant amounts of water to be present. However, conductive minerals like salt brines, mineralogical clay minerals, metallic minerals, and high temperature materials (dry geothermal) may also be highly conductive and thus confuse the search for water. Some of this could be sorted out by measuring electrical properties as a function of frequency and temperature as the bulk of the confusing mineralogies exhibit distinctive electrochemical responses [13].

To focus further on water, if low frequency measurements show a low seismic Q and a high electrical conductivity, and there is no distinctive electrochemical signature of reactive mineralogy, then the coupled process, seismoelectric method should be used. In this, a seismic wave propagates, exciting water movement (if present) inside fractures and pore spaces. The electrical charge accumulation at pore walls is carried along by flowing fluids inside the pore, requiring an electrical counter current to maintain charge neutrality. The counter current flow through a finite electrical conductivity fluid generates a voltage measured as a streaming potential [14, 15, 16]. The correlated seismic source and electrical response is a low ambiguity indicator of the presence of liquid water. If there is no response, then there is no mobile liquid water. There may be adsorbed water.

Discussion: The search for water on Mars is compounded by several factors. The high iron content soils on Mars are known from Viking and Pathfinder [17] to be magnetic at low frequencies. However, the lack of knowledge about detailed magnetic mineralogy means there is no information about their frequency and temperature dependence on Mars. The possibility exists for strong magnetic responses with high variability over frequency ranges of significance to both high and low frequency electromagnetic methods, and for high variability over diurnal and seasonal temperature ranges.

The lack of knowledge about the electromagnetic noise spectrum on Mars makes design of an adequate electromagnetic exploration system difficult.

Seismic measurements of Q are difficult on the earth, and the complete lack of successful seismic measurements on Mars leaves much to be desired, with a long list of unknowns (noise, coupling, etc.).

The alternative to deep electromagnetic and seismic exploration for water on Mars is blind drilling. Given the mass and costs of transport, and the odds of success in the face of geological heterogeneity, drilling must be preceded by adequate geophysical exploration.

In order to design an adequate geophysical exploration program for water, electromagnetic and seismic noise levels must be measured on Mars. The magnetic mineralogy must be determined and the impacts on electromagnetics must be studied. The Mars range temperature dependence of the properties of water bearing systems must be studied for the range of mineralogies expected. Seismic coupling of instruments to Mars dusts and soils under Mars ambient temperature and pressure must be studied.

At the end of these measurements and studies, the range of water contents and conditions that could be detected on Mars and over what range of geologies and depths could then be accurately predicted.

References: [1] Olhoeft, G. R. (2001) Subsurface geophysical detection methods to uniquely locate water on Mars: Conf. Geophysical Detection of Subsurface Water on Mars, LPI Publication 1095, p. 72-73. [2] Nabighian, M. N., ed. (1992) Electromagnetic methods in applied geophysics: Soc. Explor. Geophys., Tulsa, OK, 2 vols. [3] <http://www.g-p-r.com> [4] Grimm, R. E. (2001) JGR DOI 10.1029/2001JE001504. [5] Olhoeft, G. R. (1998) Ground penetrating radar on Mars: in Proc. of GPR'98, Seventh Int'l. Conf. on Ground Penetrating Radar, The University of Kansas, p. 387-392. [6] Olhoeft, G. R. (1998) Electrical, magnetic and geometric properties that determine ground penetrating radar performance: in Proc. of GPR'98, Seventh Int'l. Conf. on Ground Penetrating Radar, The University of Kansas, p. 177-182. [7] Olhoeft, G. R. (1981) Electrical properties of rocks, in Physical Properties of Rocks and Minerals, McGraw-Hill, p. 257-330. [8] Onsager, L. and Runnels, L. K. (1969) Diffusion and relaxation phenomena in ice: J. Chem. Phys., v.50, p.1089-1103. [9] Olhoeft, G.R., and Strangway, D.W. (1974) Geophysics, v. 39, p. 302-311. [10] [Bourbie et al. (1987) Acoustics of porous media: Gulf Publ. Co., 334p. [11] Mavko, G., et al. (1998) The rock physics handbook: Cambridge Univ. Press, 329p. [12] Vaniman, D., et al. (1991) The lunar environment, in Lunar Sourcebook: Cambridge Univ. Press, p. 27-60. [13] Olhoeft, G. R. (1985) Geophysics, v. 50, p. 2492-2503. [14] Pride, S. R. (1994) Phys. Rev. B, v. 50, p. 15678-15696. [15] Pengra, D.B. et al. (1999) JGR, v. 104, p. 29485-29508. [16] Zhu et al. (2000) JGR, v.105, p. 28055-28064. [17] Morris, R.V., et al. (2001) JGR, v. 106, p. 5057-5083.

Mars Electromagnetic Sounding Experiment (MARSES): Comparative and calibration studies on the example spatial and temporal variations subsurface geoelectrical sections of the saltwater interface on Sicily (Donnalucata Beach) and Shelter Island.

Y. R. Ozorovich¹, A. K. Lukomski¹, B. Zoubkov¹, F. Babkin¹

¹Space Research Institute, Russian Academy of Sciences, 84/32 Profsoyuznaya st., Moscow, 117810, Russia

Phone: 7-095-333-3177; Fax: 7-095-333-2177; e-mail: yozorovi@iki.rssi.ru.

<http://www.iki.rssi.ru/MARSES/>

The MARSES is the sounding instrument program on the base new portable geophysical instrumentation developed of searching for water, water-ice or permafrost layers existing in some depth under the visible surface of Mars. The first task is to measure the soil properties of the subsurface of Mars, which include porosity, electrical resistance of the liquid phase, thermal conductivity, temperature dependence and so on. A main task of the MARSES experiment is to examine changes in subsurface properties of local areas regolith on the martian subsurface, and to relate them to optical images and other remote sensing data in order to understand the nature of different terrain forms and structure of cryolitozone of Mars.

On the basis of results of several expedition programs in the earth's conditions the optimum configuration of devices and techniques of measurement which allows to receive spatial geoelectrical structure subsurface horizons near martian landers or rover study area in the future martian missions is revealed.

During cooperation within the frames of space research missions devoted to Mars exploration, which soil slice conditions are close to Earth's arid and semiarid lands, was developed compact, light and reliable instrument for subsurface sounding and mapping for Earth's applications, and more specifically it relates to a method to map, track, and monitoring: groundwater, groundwater channels, groundwater structures, subsurface pollution plumes, maps interconnected fracture or porous zones, map leaks in earthen dams, map leaks in drain fields, monitor changes in subsurface water flow, monitoring changes in ion concentration in groundwater, monitor in situ leaching solution, monitor movement of heap leaching solutions, monitor changes in subsurface redox or reaction fronts, monitor underground chemical reactions, monitoring subterranean bioreactions, or other subsurface water and related geological structure.

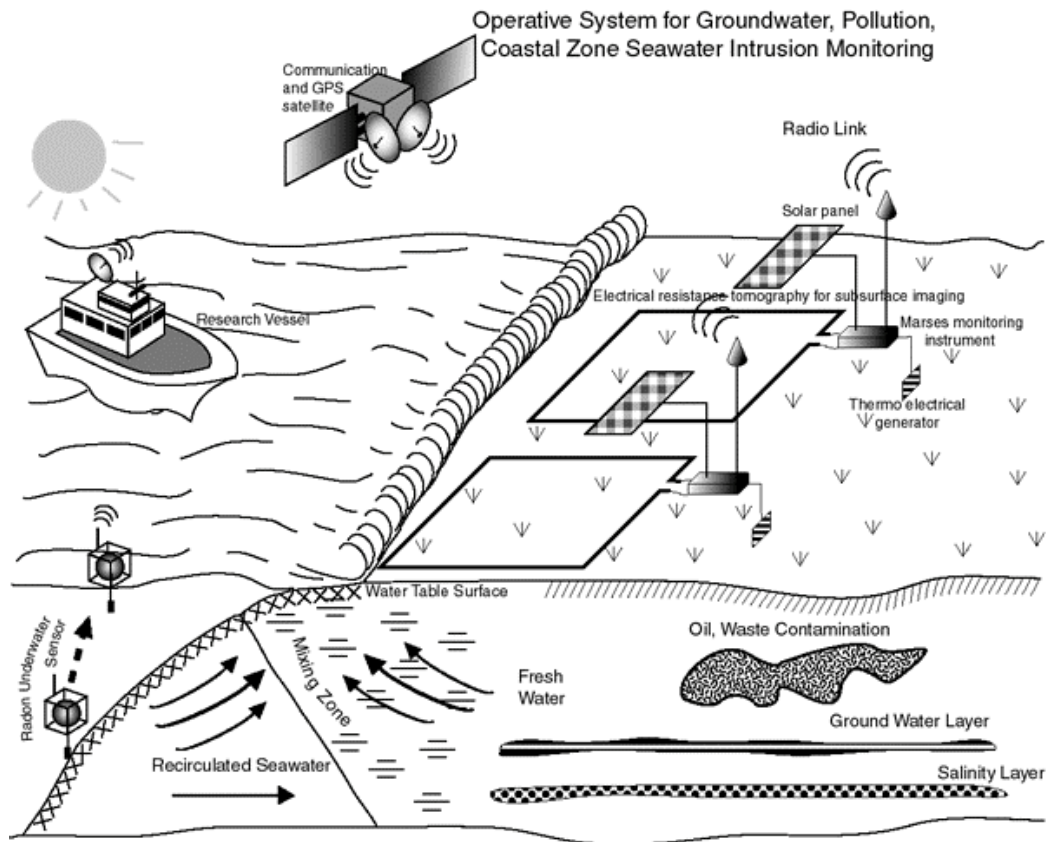


Figure 1. The subsurface monitoring system organization structure.

First observations of the dynamic parameters (spatial and temporal variations and changes of the salt/water interface in the process of the inland extent and movement of saltwater interface up to sounding depth in order to 100 m) have been obtained on the base new generation non-invasive instrument for subsurface sounding and new methodology . This is comparative and calibration studies is very important for future experiment on the surface of Mars and also for many application on the Earth .

Operative geophysical survey of the saltwater and freshwater interaction is an urgent task for operative monitoring subsurface system in drylands area in variuos regions of the world for long-term monitoring nature subsurface ecosystem.

Building of geographical slice using different instruments allows to obtain correct parameters for MARSES TEM in order to employ it in frozen soils sounding on the surface of Mars and for many applications for long-term monitoring and subsurface studies in the Earth's conditions.

References:

- [1] Clifford S.M. (1993) *JGR*, 98, 10973–11016. [2] Toulmin P.,*et al*, (1977) *JGR*,82,4624-4634 [3] Fanale F.P. (1986) *Icarus*, 67,1-18.[4] Kuzmin R.O.,*et al*,(1988) *LPS Conf.XIX Abstracts*,657-658 [5]Ozorovich Y.R.,*et al*,(1988) Tentative of e/m sounding (low-frequency) sounding cryolithozone of Mars, Preprint IKI, No.1477 [6]Ozorovich Y.R., *et al*,(1988) Microwave remote sensing of martian subsurface parameters, Preprint IKI,No.1531. [7] Ozorovich Y.R., *et al*, (1999) Mars Electromagnetic Sounding Experiment - MARSES, Proceedings of LPSC, March 15-19,1999. [8] Ozorovich Y.R., *et al*, (2000) **Possibilities of using MARSES instrument for long-term monitoring and subsurface studies in arctic and arid lands** , Proceedings of LPSC, March, 2000.